

Efficient systematic scheme to construct second-principles lattice-dynamical models

Carlos Escorihuela-Sayalero,¹ Jacek C. Wojdeł,² and Jorge Íñiguez^{1,2}

¹*Materials Research and Technology Department,
Luxembourg Institute of Science and Technology (LIST),*

5 avenue des Hauts-Fourneaux, L-4362 Esch/Alzette, Luxembourg

²*Institut de Ciència de Materials de Barcelona (ICMAB-CSIC), Campus UAB, 08193 Bellaterra, Spain*

We start from the polynomial interatomic potentials introduced by Wojdeł *et al.* [J. Phys. Condens. Matt. **25**, 305401 (2013)] and take advantage of one of their key features – namely, the linear dependence of the energy on the potential’s adjustable parameters – to devise a scheme for the construction of first-principles-based (*second-principles*) models for large-scale lattice-dynamical simulations. Our method presents the following convenient features. The parameters of the model are computed in a very fast and efficient way, as it is possible to recast the fit to a training set of first-principles data into a simple matrix diagonalization problem. Our method selects automatically the interactions that are most relevant to reproduce the training-set data, by choosing from a pool that includes virtually all possible coupling terms, and produces a family of models of increasing complexity and accuracy. We work with practical and convenient cross-validation criteria linked to the physical properties that will be relevant in future simulations based on the new model, and which greatly facilitate the task of identifying a potential that is simultaneously simple (thus computationally light), very accurate, and predictive. We also discuss practical ways to guarantee that our energy models are bounded from below, with a minimal impact on their accuracy. Finally, we demonstrate our scheme with an application to ferroelastic perovskite SrTiO₃, which features many non-trivial lattice-dynamical features (e.g., a phase transition driven by soft phonons, competing structural instabilities, highly anharmonic dynamics) and provides a very demanding test.

I. INTRODUCTION

Over the past decades first-principles simulation methods have undergone a fantastic transformation, from a rather specialized technique reserved to a few groups to a standard and powerful tool accessible to any research team in the world. In particular, methods based on efficient schemes like Density Functional Theory (DFT) [1, 2] make it possible to run predictive simulations of many materials and systems [3]. However, because of the finite computer power, DFT studies are still limited to relatively small simulation boxes of a few hundreds of atoms; further, except in the simplest of cases, computing statistical averages in realistic conditions is all but impossible. These limitations can be partly overcome by introducing effective models, with parameters computed from first principles, that permit faster and larger-scale calculations (e.g., statistical or dynamical, including thousands of atoms) while retaining, to some extent, first-principles predictive power and accuracy [4]. In the following we refer to such approaches as *second-principles* methods, adopting the terminology coined in Ref. 5.

While progress in second-principles simulations has been impressive, this is still an emerging field, and the present situation is somewhat comparable to that of DFT methods about three decades ago. The effective models and corresponding simulation tools are reasonably well established in some particular contexts, as e.g. for the study of proteins and other biological systems [6]. However, we are still far from having general tools that permit a non-specialist to tackle a new problem. The current challenge is to bring the second-principles techniques to

the level that DFT simulation has reached.

This is a daunting endeavor, much complicated by the fact that, by their own nature, different second-principles methods may rely on utterly diverse approximations. Even if we restrict ourselves to atomistic schemes, we can distinguish between approaches that treat explicitly both atoms and electrons, and those in which only the atoms are retained in the description. Among the latter, we can find a wealth of options to handle the interatomic interactions, ranging from physically or chemically motivated models (which range from the very simple – as the Lennard-Jones [7] or bond-valence [8–10] potentials – to the quite complex – as e.g. the so-called *ReaxFF* force fields [11]) to abstract mathematical approaches (e.g., those based on neural networks [12]). Different schemes present different strengths and weaknesses, and adapt better to different problems. For example, a suitable method to tackle phenomena that involve formation and breaking of chemical bonds (e.g., *ReaxFF*) may not be the most appropriate to handle relatively simpler situations (e.g., those in which the bonding topology is preserved) that may nevertheless require a high quantitative accuracy.

Here we focus on the latter category, i.e., on cases in which an underlying lattice of chemical bonds can be assumed to remain essentially unperturbed throughout the simulation. While this *constant-topology* condition may look restrictive at first, there are many all-important properties that are perfectly compatible with it, including most lattice-dynamical phenomena, lattice thermal transport, dielectric and piezoelectric responses, and even structural phase transitions driven by soft phonon modes. Wojdeł *et al.* [13] took advantage of

this constant-topology assumption to introduce simple and general polynomial potentials that describe the dependence of the energy – written as a Taylor series around a suitable reference structure – on arbitrary (though relatively small) atomic distortions. Indeed, in Ref. 13 some of us showed that such potentials provide a very flexible framework to fit accurately a training set of first-principles data. In particular, this approach allowed us to resolve the temperature-driven phase transitions of prototypical ferroelectric (PbTiO_3 or PTO) and ferroelastic (SrTiO_3 or STO) perovskite oxides [13]; further, it has allowed us to discover effects – ranging from novel structural phases under elastic constraints [13], to the occurrence of ferroelectric phase transitions within the ferroelectric domain walls of PTO [14], or the negative-capacitance behavior of the PTO layers of PTO/STO superlattices [15] – that had been essentially missed by previous effective models or direct DFT simulations. Hence, the methods of Ref. 13 have amply proven their usefulness and deserve further development.

In this article we report our recent work based on the approach of Ref. 13, and introduce key developments in the way in which the models are constructed. The original work [13] was based on a somewhat primitive (perfectly standard) algorithm that required us to choose the interaction terms of the model before fitting the parameters to a training set of DFT data; then, the fitting process involved successive (and computationally costly) constrained optimizations based on the minimization of non-linear goal functions. This scheme is good enough to produce useful models, but it is far from optimal. In particular, it does not take advantage of some unique features of our potentials that permit a far more efficient and powerful approach.

Here we introduce a model-construction procedure that automatically identifies the most relevant coupling terms and computes the corresponding parameters. The most important terms are selected from a pool that may be defined to include virtually all possible interatomic interactions, of the order of hundreds in the applications considered in this work. Our scheme is designed to produce a *family* of models of increasing complexity and accuracy; thus, it makes it possible to choose the potential better suited to specific investigations. (Naturally, the computational burden of the ensuing statistical or dynamical simulations grows with the complexity or size of the potential.) Such an exhaustive model-construction procedure relies on a very fast and efficient algorithm for the calculation of the model parameters: In essence, we recast the usual (costly and cumbersome) optimization problem into one that involves solving (almost instantaneously) a system of linear equations. This critical step is possible thanks to a distinct feature of our polyno-

mial models, namely, that the energy depends linearly on the parameters to be fitted. Thus, in summary, our new method makes it possible to obtain models of exceedingly high accuracy in a fast and robust way.

The paper is organized as follows. In Section II we introduce the formalism behind the new model-construction scheme, and also address issues concerning cross-validation and energy boundedness. In Section III we describe the construction of models for STO, a challenging material to test our method. Different possibilities to construct a training set and fit the model parameters, as well as other practical aspects, are discussed in some detail. Finally, in Section IV we summarize our work.

II. FORMALISM

In this section we describe our approach in a material-independent way. First we review the model-potential scheme of Ref. 13, recalling the basic formulas and notation. Then we describe our present strategy for an automatic model construction, which takes advantage of the linearity of the potential with respect to the fitting parameters. Finally, we introduce the problem of cross-validating the models, and also mention briefly the question of how to obtain potential energies that are bounded from below; these practical issues will be better explained with an example in Section III.

A. Second-principles lattice-dynamical models

The models proposed by Wojdel *et al.* [13] can be described as a Taylor series of the energy, around a certain reference structure (RS), as a function of atomic displacements (\mathbf{u}) and strains ($\boldsymbol{\eta}$). It is convenient to split the energy $E(\mathbf{u}, \boldsymbol{\eta})$ in three parts:

$$E(\mathbf{u}, \boldsymbol{\eta}) = E_{\text{RS}} + E_{\text{p}}(\mathbf{u}) + E_{\text{s}}(\boldsymbol{\eta}) + E_{\text{sp}}(\mathbf{u}, \boldsymbol{\eta}), \quad (1)$$

where the subscripts “p”, “s” and “sp” stand for “phonon”, “strain”, and “strain-phonon”, respectively, and E_{RS} is the energy of the reference configuration. We assume the typical case in which the RS is a critical point of the PES, so that the first-order terms of the Taylor series vanish. Further, following Ref. 13, we write the energy in terms of displacement differences, so that our potential is explicitly compliant with the acoustic sum rule at all orders of the expansion. Using Latin letters to label the atoms in our material and Greek letters to label Cartesian coordinates, we can write the following general expression for E_{p} :

$$E_{\text{p}}(\mathbf{u}) = \frac{1}{2} \sum_{\substack{ijkh \\ \alpha\beta}} \tilde{K}_{ij\alpha kh\beta}^{(2)} (u_{i\alpha} - u_{j\alpha})(u_{k\beta} - u_{h\beta}) + \frac{1}{6} \sum_{\substack{ijkhrt \\ \alpha\beta\gamma}} \tilde{K}_{ij\alpha kh\beta rt\gamma}^{(3)} (u_{i\alpha} - u_{j\alpha})(u_{k\beta} - u_{h\beta})(u_{r\gamma} - u_{t\gamma}) + \dots, \quad (2)$$

where the $\tilde{\mathbf{K}}^{(n)}$ tensors can be related with the n -th derivatives of the energy,

$$K_{ijk\dots\alpha\beta\gamma\dots}^{(n)} = \frac{\partial^n E}{\partial u_{i\alpha} \partial u_{j\beta} \partial u_{k\gamma} \dots}, \quad (3)$$

by expanding the displacement-difference products in Eq. (2). Analogously, we write the strain-phonon term as

$$E_{\text{sp}}(\mathbf{u}, \boldsymbol{\eta}) = \frac{1}{2} \sum_a \sum_{ij\alpha} \tilde{\Lambda}_{aij\alpha}^{(1,1)} \eta_a (u_{i\alpha} - u_{j\alpha}) + \frac{1}{6} \sum_a \sum_{ijkh} \sum_{\alpha\beta} \tilde{\Lambda}_{aij\alpha kh\beta}^{(1,2)} \eta_a (u_{i\alpha} - u_{j\alpha}) (u_{k\beta} - u_{h\beta}) + \dots, \quad (4)$$

where $\tilde{\Lambda}^{(m,n)}$ is the coupling tensor of order m in strain and n in the atomic displacements, and we use Latin letters (a, b , etc.) to label strain components in Voigt notation [16]. Finally we have

$$E_s(\boldsymbol{\eta}) = \frac{N}{2} \sum_{ab} C_{ab}^{(2)} \eta_a \eta_b + \frac{N}{6} \sum_{abc} C_{abc}^{(3)} \eta_a \eta_b \eta_c + \dots, \quad (5)$$

where $\mathbf{C}^{(m)}$ is the bare elastic tensor of order m . Note that when working with insulators (as in the example that will be described below), it is convenient to further split the interactions involving phonons in long-range (dipole-dipole) and short-range parts [13, 17].

The expression for the energy gives us access to all relevant lattice-dynamical quantities; in particular, the forces on the atoms are given by

$$f_{i\alpha} = - \left. \frac{\partial E}{\partial u_{i\alpha}} \right|_{\mathbf{u}, \boldsymbol{\eta}} \quad (6)$$

for a certain $(\mathbf{u}, \boldsymbol{\eta})$ configuration, while the stresses acting on the cell are

$$\sigma_a = - \left. \frac{\partial E}{\partial \eta_a} \right|_{\mathbf{u}, \boldsymbol{\eta}}. \quad (7)$$

Note that, in order to match the usual definition of stress, this derivative needs to be computed under the condition that the *relative* positions of the atoms in the cell are kept constant. This is not direct in our scheme, as we work with absolute atomic displacements \mathbf{u} ; nevertheless, in practice this derivative calculation can be easily tackled by implementing an appropriate chain rule.

B. Calculation of model parameters

There is a standard procedure to compute the parameters of a lattice-dynamical model, directly applicable to any potential type, including ours. The objective is to

obtain a model that reproduces a *training set* (TS) of relevant lattice-dynamical and structural data. To quantify the model's accuracy in reproducing the TS, one introduces a positively defined *goal function* (GF), and turns the parameter fitting into a GF minimization problem. Solving this problem is typically a hard task, as the GF is usually a high-dimension non-linear function of the free parameters, with an intricate multi-minima landscape associated to it. Hence, a time-consuming numerical solution is mandatory in most cases. In essence, this is the approach some of us adopted in Ref. 13.

Here we show that, because of the particular form of our interaction potentials, we can make a judicious choice of GF that permits an analytic solution to the parameter-fitting problem. This is a drastic simplification that allows for very fast parameter calculations, which in turn makes it possible to implement an automatic procedure to identify the best model from essentially all possible couplings.

1. Definitions and goal function

As it is obvious from the formulas above, our models are linear in the parameters to be fitted. Hence, we can formally write the energy of a model with p parameters as

$$E[\Theta_p](\mathbf{u}, \boldsymbol{\eta}) = \sum_{\lambda} \theta_{\lambda} t_{\lambda}(\mathbf{u}, \boldsymbol{\eta}) + E^{\text{fixed}}(\mathbf{u}, \boldsymbol{\eta}), \quad (8)$$

where $\Theta_p := \{\theta_1, \dots, \theta_p\}$ is the set of free parameters and $\mathcal{T}_p := \{t_1, \dots, t_p\}$ gathers the corresponding polynomial terms. Note that for a given parameter θ_{λ} , the corresponding t_{λ} includes *all* the symmetry-related terms (i.e., all products of atomic displacements and strains) whose coupling is given by θ_{λ} . We call t_{λ} a symmetry-adapted term (SAT), using the terminology of Ref. 13. For convenience, we also introduce an energy E^{fixed} that gathers all the terms that do not need to be fitted. E^{fixed} will typically include interactions that can be computed from

first principles in a straightforward way, such as the harmonic bare elastic constants, the harmonic dipole-dipole couplings, etc.

Now we introduce a goal function $G[\Theta_p]$ that (1) is aimed at constructing models that give a good description of lattice-dynamical properties and (2) is a simple function of the model parameters. It is most natural and convenient to choose a GF of the form

$$G[\Theta_p, \text{TS}] = \frac{1}{M_1} \sum_{s\tau} (f_\tau^{\text{TS}}(s) - f_\tau[\Theta_p](s))^2 + \frac{1}{M_2} \sum_{sa} \Omega^2(s) (\sigma_a^{\text{TS}}(s) - \sigma_a[\Theta_p](s))^2, \quad (9)$$

where s labels the M configurations in the TS and we have introduced the bijective mapping $i\alpha \leftrightarrow \tau$ to alleviate the notation. Note that we mark the target forces and stresses with a “TS” superscript, and we also indicate the parametric nature of the quantities derived from the model. M_1 and M_2 are normalization factors computed as the cardinal of the elements of the corresponding sums. $\Omega(s)$ is the factor that Sheppard *et al.* [18] proposed, in the context of nudged-elastic-band calculations, to properly weight forces and stresses; it is defined as

$$\Omega(s) = \left(V(s) \sqrt{N} \right)^{-1/3}, \quad (10)$$

where N is the number of atoms in the simulation cell and $V(s)$ the cell volume for configuration s .

2. Analytic minimum of the goal function

Let us denote the SAT derivatives with respect to atomic displacements and strains by

$$\bar{f}_{\lambda\tau}(s) = - \frac{\partial t_\lambda(\mathbf{u}, \boldsymbol{\eta})}{\partial u_\tau} \bigg|_s \quad (11)$$

and

$$\bar{\sigma}_{\lambda a} = - \frac{\partial t_\lambda(\mathbf{u}, \boldsymbol{\eta})}{\partial \eta_a} \bigg|_s, \quad (12)$$

respectively. Then, the forces and stresses computed as derivatives of Eq. (8) can be written as

$$f_\tau(s) = \sum_\lambda \theta_\lambda \bar{f}_{\lambda\tau}(s) + f_\tau^{\text{fixed}}(s) \quad (13)$$

and

$$\sigma_a(s) = \sum_\lambda \theta_\lambda \bar{\sigma}_{\lambda a}(s) + \sigma_a^{\text{fixed}}(s), \quad (14)$$

respectively, where $f^{\text{fixed}}(s)$ and $\sigma^{\text{fixed}}(s)$ are the corresponding derivatives of E^{fixed} evaluated at configuration s . Hence, the GF can be rewritten as

$$G[\Theta_p, \text{TS}] = \frac{1}{M_1} \sum_{s\tau} \left(f_\tau^{\text{TS}}(s) - \sum_\lambda \theta_\lambda \bar{f}_{\lambda\tau}(s) - f_\tau^{\text{fixed}}(s) \right)^2 + \frac{1}{M_2} \sum_{sa} \Omega^2(s) \left(\sigma_a^{\text{TS}}(s) - \sum_\lambda \theta_\lambda \bar{\sigma}_{\lambda a}(s) - \sigma_a^{\text{fixed}}(s) \right)^2. \quad (15)$$

The extrema of the goal function satisfy $\partial G[\Theta_p, \text{TS}] / \partial \theta_\mu = 0 \ \forall \mu$. This translates into the set of conditions

$$\frac{2}{M_1} \sum_{s\tau} \left(f_\tau^{\text{TS}}(s) - \sum_\lambda \theta_\lambda \bar{f}_{\lambda\tau}(s) - f_\tau^{\text{fixed}}(s) \right) \bar{f}_{\mu\tau}(s) + \frac{2}{M_2} \sum_{sa} \Omega^2(s) \left(\sigma_a^{\text{TS}}(s) - \sum_\lambda \theta_\lambda \bar{\sigma}_{\lambda a}(s) - \sigma_a^{\text{fixed}}(s) \right) \bar{\sigma}_{\mu a}(s) = 0, \quad (16)$$

for $\mu = 1, \dots, p$. This expression can be recast in the following, more convenient form

$$\sum_\lambda \left[\sum_s \left(\frac{1}{M_1} \sum_\tau \bar{f}_{\mu\tau}(s) \bar{f}_{\lambda\tau}(s) + \frac{1}{M_2} \sum_a \Omega^2(s) \bar{\sigma}_{\mu a}(s) \bar{\sigma}_{\lambda a}(s) \right) \right] \theta_\lambda = \sum_s \left(\frac{1}{M_1} \sum_\tau [f_\tau^{\text{TS}}(s) - f_\tau^{\text{fixed}}(s)] \bar{f}_{\mu\tau}(s) + \frac{1}{M_2} \sum_a \Omega^2(s) [\sigma_a^{\text{TS}}(s) - \sigma_a^{\text{fixed}}(s)] \bar{\sigma}_{\mu a}(s) \right), \quad (17)$$

which we can further simplify to write

$$\sum_{\lambda} \Delta_{\mu\lambda} \theta_{\lambda} = \Gamma_{\mu}, \quad (18)$$

where $\Delta_{\mu\lambda}$ and Γ_{μ} are trivially defined by comparing Eqs. (17) and (18). Hence, we can find the extrema of $G[\Theta_p]$ by solving a system of p linear equations.

Our GF can be viewed as a p -dimensional parabola, and we always have $G[\Theta_p, \text{TS}] \geq 0$. Further, as shown in Appendix A, the eigenvalues of the associated Hessian ($H_{\lambda\mu} = \partial^2 G / \partial \theta_{\lambda} \partial \theta_{\mu}$) are either positive or zero. It is thus clear that a critical point of G must be a minimum, never a saddle point or maximum. (Note that, by definition, a saddle point requires the presence of both positive and negative eigenvalues.)

It is also relatively easy to show (see Appendix A) that, for a specific choice of Θ_p and TS, we can have two possible scenarios: either Eq. (18) has a single solution or it has infinite ones. The former case corresponds to the situation in which there exists a well-defined collection of values of the Θ_p parameters yielding an optimum compromise to reproduce the TS data. (All the Hessian eigenvalues are positive in this case, and the solution of Eq. (18) is a minimum of G .) The latter case corresponds to the situation in which the solution of Eq. (18) is a manifold with dimension greater than zero, implying that some linear combinations of parameters can take arbitrary values without affecting G . Such combinations correspond to Hessian eigenvectors with zero eigenvalue; G does not have a single minimum, but a manifold of minima, in this case.

It is interesting to note the reasons why there may be linear dependencies in our system of equations. Let us consider $\Delta_{\mu\lambda}$ and Γ_{μ} in Eq. (18); these are p -dimensional objects that encapsulate all the information in the TS in a compact way. In the limit of a large p and a relatively small TS, it may happen that the TS does not provide enough information to fit all the parameters in Θ_p . In such a case, the system of equations will be underdetermined, yielding infinite solutions. A similar difficulty appears when the TSs are obtained in ways that only explore a subset of the configuration space, e.g., most typically, by running molecular dynamics (MD) simulations in relatively small supercells. In such a case, the periodic boundary conditions associated with the employed supercell effectively define the spatial range of the interatomic couplings that can be resolved. Indeed, as far as the description of the TS data is concerned, and as sketched in Fig. 1, interactions extending beyond that supercell-defined distance become exactly equivalent to other shorter-range couplings. Hence, they lead to linear dependencies when setting up the system of equations in Eq. (18).

In practice, it is easy to handle the situations in which Eq. (18) has infinite solutions. On one hand, if we believe our TS is complete enough, the presence of infinite solutions suggests that we can simplify our model without loss of accuracy. We can do so in an orderly and

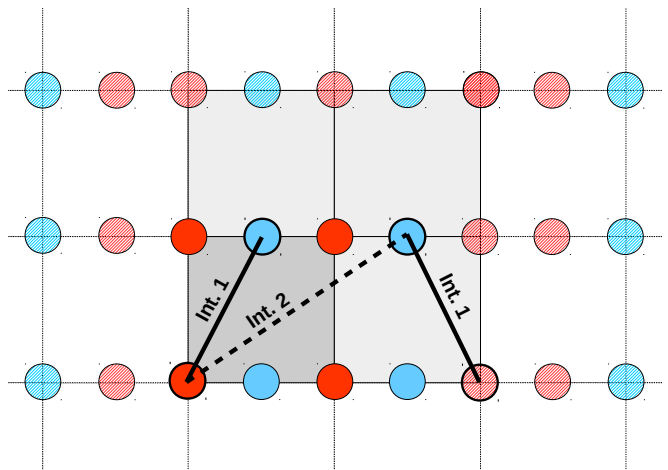


FIG. 1. Sketch illustrating how the choice of a supercell for the generation of the TS data implicitly imposes a spatial cutoff for the interatomic interactions. The elemental unit cell of the crystal is colored in dark grey, while the supercell used for the TS calculations is in light grey. The elemental cell contains two atoms. The atoms in the supercell are displayed in strong colors, while their periodic images are shaded. The interactions labeled as “Int. 1” and “Int. 2” are obviously different, but they cannot be resolved on the basis of data obtained for this supercell. Note that the longest-range “Int. 2” connects atoms that are also linked by “Int. 1” due to the periodic supercell repetition.

physically-motivated way, e.g., by removing from Θ_p the longest-range interactions that lead to linear dependencies in Eq. (18). On the other hand, if we are interested in quantifying precisely all the interactions in our model, the presence of infinite solutions indicates that we need to extend the TS so as to remove the linear dependencies. In this case, we will typically need to include information that is qualitatively different from that in the original TS, e.g., obtained from MD simulations of larger supercells, etc.

3. Finding the best model of p terms

We are interested in constructing models that are accurate and, at the same time, permit fast calculations. Hence, we need to find a way to construct the simplest (computationally lightest) models that reproduce the TS with a certain accuracy. Naturally, we can use the goal function as the measure of accuracy, so that the above problem translates into finding the simplest model whose associated GF is below a certain threshold. (As we will see in Section III, in order to evaluate a model’s accuracy and predictive power, we will eventually adopt a practical approach that goes beyond evaluating the GF.)

Let \mathcal{T}_P be the set of P terms, with associated parameters Θ_P , that define *all* the possible interactions in our material of interest. Given the specific form of our interatomic potentials, \mathcal{T}_P can be easily defined by three ap-

proximations or cutoffs: the maximum order of the polynomial, the maximum spatial range of the interactions, and the maximum number of bodies in the interaction terms. For specific choices of these three cutoffs, one can implement an algorithm that identifies all the SATs the model can potentially contain. We will typically have a very large number of them, of the order of $P = 500$ in the application discussed below.

Let us use the expression *p-model* to refer to a model of p terms, $\mathcal{T}_p \subset \mathcal{T}_P$ and $\Theta_p \subset \Theta_P$ being the corresponding sets of terms and parameters, respectively. We need a way to find the best p -model, i.e., the choice of \mathcal{T}_p and Θ_p that minimizes the GF when we restrict ourselves to models of p terms. A brute-force approach to this search – by computing all possible p -models and comparing the corresponding GF values – would be a daunting task. For example, for a representative case of $P = 500$ and $p = 20$, we have about 10^{35} different models. Obviously, in spite of our efficient strategy to compute the parameters for an specific choice of \mathcal{T}_p , considering so many possibilities is computationally unfeasible.

We overcome this difficulty by constraining the model search, implementing what can be described as a *stepwise procedure with forward selection* [19]. In short, we start with $p = 1$ and identify the best 1-model, a problem that we solve exactly by considering all P possible candidates. Let \mathcal{T}_1^* denote the best 1-model. Then, we move to $p + 1$ and consider all possible \mathcal{T}_{p+1} models subject to the constraint that $\mathcal{T}_p^* \subset \mathcal{T}_{p+1}$. In other words, we only consider $p+1$ -models that contain the terms of the best p -model. We can solve this problem exactly, by considering all $P - p$ possibilities explicitly. Then we iterate the procedure until a sufficiently small GF is obtained.

We have checked the reliability of the above procedure in two ways. First, for a number of \mathcal{T}_P choices with small P , we run a brute-force search for the best p -models, and compare the exact results thus obtained with the outcomes of our proposed strategy. In essence, our constrained approach succeeds in identifying the best p -model in almost all cases, and the very few exceptions correspond to cases with very small values of p (in our work with STO, we find this problem for $p < 5$, a limit where the corresponding models are not physically sound anyway). Second, we consider the following refinement of our algorithm: once \mathcal{T}_p^* has been identified, we check whether it is possible to improve the GF by replacing one of the chosen p terms by one of the remaining $P - p$. We find that such a refinement seldom improves the best p -model, and the few cases in which an improvement is observed correspond to very small p values.

C. Cross-validation

In Statistics, *cross-validation* is a common procedure to analyze the predictiveness of a model, and is often used as *stopping criterion* in model construction methodologies.

A rather usual approach to it is the so-called *leave-n-out* method [20]. This method consist in the following steps. Given a TS, we remove from it n randomly selected elements, and fit the best p -model to the remaining elements by minimizing the GF. Let $G(p)$ denote the resulting GF value. Then, we test the accuracy of such best p -model by evaluating the GF using the n TS elements left out of the fit. Let $G^{\text{test}}(p)$ denote the resulting GF value. Naturally, we expect $G(p) > G(p + 1)$ and $G^{\text{test}}(p) > G^{\text{test}}(p + 1)$, as models should improve as they become more complex. Then, if we find p^{best} such that $G^{\text{test}}(p^{\text{best}}) < G^{\text{test}}(p^{\text{best}} + 1)$, this indicates that our model is loosing predictive power as it grows, and we can thus identify the optimum size ($p = p^{\text{best}}$) of the model.

Unfortunately, in actual applications this procedure tends to render $G^{\text{test}}(p)$ curves that display several minima, making it difficult to identify the most predictive model [21]. In our particular case, as we detail below, we find a different complication: We work with well-populated TSs constructed from MD trajectories, and the TS elements (i.e., the atomic configurations representative of the trajectory) tend to contain similar information; hence, our calculated $G^{\text{test}}(p)$ curves do not present any minimum. As we will see below, we resolve this difficulty by creating a physically-motivated test set that allows us to perform a convincing cross-validation and verify that our models will be reliable for the calculation of properties of interest.

D. Energy boundedness

Before concluding this section, we should note the main weakness of the approach just described, namely, that the energy of our optimum models is likely to be unbounded from below.

Our scheme involves running an unconstrained search for the best p -model, testing polynomial terms from a pool \mathcal{T}_P that essentially includes all possible couplings compliant with cutoffs concerning the order of the expansion, the spatial range of the interactions, and the number of bodies in the interacting terms. The behavior of the model for large atomic distortions is dominated by the highest-order terms, which are not guaranteed to be positive definite. In other words, nothing in our construction scheme prevents the models from presenting run-away solutions with $E \rightarrow -\infty$.

Naively, one could expect that a complete enough TS will automatically produce bounded models. More precisely, high-energy atomic configurations, involving large distortions of the RS, provide information about the restoring forces that keep the atoms together; hence, in order to tackle the unboundedness problem, it may seem sufficient to include representative configurations of that sort (e.g., as obtained from high-temperature MD runs) in the TS. Unfortunately, our experience indicates that this procedure is not enough to constrain all possible run-

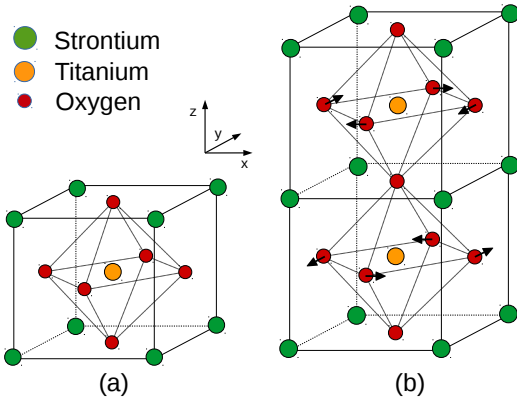


FIG. 2. Sketch of the STO perovskite structure. Panel (a) shows the elemental cell for the high-symmetry cubic ($Pm\bar{3}m$) structure. Panel (b) sketches the antiphase O_6 rotations that characterize the AFD distortion driving the structural phase transition in STO.

away directions in the general case and, thus, it does not lead to an automatic model-generation scheme.

In this work we have considered a number of possible, potentially-automatic solutions to this problem, briefly described below. These experiments have led us to identify a practical strategy that, while requiring some inspection of the best models (i.e., while it is not fully automatic as implemented at present), appears as a satisfactory compromise, allowing to impose boundedness without any significant loss of accuracy.

III. APPLICATION TO SrTiO_3

We have chosen SrTiO_3 as our test material. STO is one of the most interesting perovskite oxides, and it has been receiving continued attention for years because of its critical importance to the field (as, e.g., it is the most widely used substrate on which thin films of other perovskites are grown [22]) and the unique physical effects it displays either in combination with other materials (e.g., exotic two-dimensional electron gas at the interface of STO with LaAlO_3 [23], novel ferroelectric effects at superlattices of STO with PTO [15, 24]) or by itself (e.g., polar order at the ferroelastic domain walls of STO at low temperatures [25, 26]). This wealth of interesting properties is partly due to STO's unique and challenging lattice-dynamical behavior, which turns this compound into an unique test case for our automatic potential-construction method. Our conjecture is that, if our scheme allows us to tackle STO successfully, it will probably allow us to investigate other, relatively simpler compounds as well.

STO crystallizes in the perovskite structure, sketched in Fig. 2. It displays a cubic phase (with $Pm\bar{3}m$ space group) at high temperatures [Fig. 2(a)], but transforms into a so-called antiferrodistortive (AFD) structure

[Fig. 2(b)] when the temperature falls below $T_C = 110$ K [27, 28]. This low-temperature phase has a tetragonal symmetry ($I4/mcm$), featuring concerted rotations of the oxygen octahedra about one of the principal axes of the perovskite lattice. Such rotations are modulated in antiphase when we move from cell to cell along the direction of the rotation axis, and the resulting structure is usually labeled $a^0a^0c^-$ in the notation introduced by Glazer [29]. [In the following we will assume that the rotation axis lies along the z direction, as shown in Fig. 2(b).]

Another interesting feature of STO is its *quantum paraelectric* character [30]. On top of the mentioned AFD structural instabilities (soft phonon modes) that drive the transition between the cubic and tetragonal phases, experiments [30] and first-principles theory [31] indicate that the cubic phase of STO presents yet another unstable distortion, namely, a polar mode whose condensation would create a macroscopic electric polarization. The reason why this spontaneous polarization is not observed experimentally in bulk STO samples is two-fold. On one hand, such a ferroelectric (FE) soft mode competes with the AFD instability, and the occurrence of the latter tends to stabilize the former [32]. On the other hand, quantum fluctuations prevent the condensation of the weakened FE instability [31]. The presence of such quantum effects (which rely on the wave-like character of the relatively-heavy atoms in STO) has been amply demonstrated theoretically and experimentally, their most obvious fingerprint being the anomalous behavior of the dielectric constant of STO at low temperatures (see Ref. 30 for experiments on STO, and Ref. 33 for simulation results for another representative quantum paraelectric, KTaO_3).

The present work focuses on the construction of effective potentials that accurately reproduce the PES of a material as obtained from first principles. Hence, a detailed comparison of the predictions of such potentials with the experimental observations is secondary in this context. In the case of our application to STO, we will solve our best models by means of *classical* Metropolis Monte Carlo (MC) simulations [34], with the purpose of verifying that we obtain the correct qualitative behavior and investigating how details of the potential affect an all-important feature, i.e., the phase-transition temperature T_C . However, while we will briefly comment on the relation between our results and the known facts about STO, a quantitative comparison with experiment is not pertinent. Indeed, because our simulations are classical, they do not include the quantum effects that strongly affect the behavior of STO at temperatures around and below the phase transition. A more detailed investigation of STO's properties, as predicted by our models and in connection with experiment, remains for future work.

A. Details of the first-principles calculations

To generate our TS data, we use DFT within the local density approximation (LDA) as implemented in the VASP package [35]. The choice of LDA over other energy functionals is not trivial. On one hand, it is known that LDA overbinds, predicting equilibrium volumes that are generally smaller than the experimental ones by 1-2%, and that this error can have a dramatic influence in the PES of materials like STO, which are very reactive to applied stresses. Hence, the LDA may not be the most appropriate choice if we are aiming at reproducing STO's experimental behavior with quantitative accuracy. On the other hand, there is an ample literature on STO modeling, including the construction of coarse-grained effective potentials [31, 36], based on LDA results. Hence, using the LDA allows us to make a more direct comparison with those previous theoretical works – including the STO model that some of us developed in Ref. 13 –, which is the most important consideration in the context of this work.

Further details of our LDA calculations are as follows. We treat the ionic cores using the projector-augmented wave method [37, 38], and solve explicitly for the following electrons: Sr's 3s, 3p, and 4s; Ti's 3s, 3p, 4s, and 3d; and O's 2s and 2p. The electronic wave functions are represented in a plane-wave basis truncated at 500 eV. Brillouin zone integrals are computed in a grid of $6 \times 6 \times 6$ k -points for calculations involving the 5-atom perovskite cell as periodically-repeated unit, or equivalent meshes when larger supercells are used. We have checked that these calculation conditions render results that are sufficiently accurate for our purposes.

Structural minimizations are run until residual force components are below 0.01 eV/Å. Langevin molecular dynamics simulations are run using the Parrinello-Rahman scheme [39, 40], to allow fluctuations of the cell volume and shape at zero applied pressure. The Langevin parameters are chosen to obtain a fast approach to the targeted temperature and reduce fluctuations. (Since we are not interested in obtaining converged equilibrium properties, the details of the Langevin dynamics are not critical.) The MD runs are always initialized with random velocities, and the atomic motions are unconstrained (thus, no symmetries are preserved). We typically use a time step of 2 fs.

B. Definition of the best possible model

As done in Ref. 13, and customary in theoretical works on ferroelectric and dielectric perovskites [32, 36, 41–43], we choose as our RS the cubic phase of the material, as obtained from a symmetry-constrained structural relaxation using the LDA. The high symmetry of this phase (full cubic $Pm\bar{3}m$ group) drastically reduces the number of allowed independent couplings in our polynomial expansion, which simplifies the task of parameter fitting.

The relevant PES of STO is characterized by relatively small atomic distortions; indeed, when we compare the cubic (RS) and tetragonal (ground state) structures, we find that the maximum change in bond distances is about 0.16 Å, corresponding to Sr–O pairs. Additionally, we know that the cubic phase is unstable against various structural distortions (most notably, the AFD modes driving the transition to the low-temperature structure), which implies that the harmonic part of the PES is not bounded from below. Given these facts, we decided to consider a 4-th order Taylor series as the simplest possible theory that is physically sound for STO, as in particular it permits energy boundedness from below.

As regards the purely elastic part of the model, we adopt the simplest possible approximation and include only harmonic terms. This choice seems both accurate (as the strains involved in STO's structural phase transition are relatively small, below 0.5 %) and sufficient to produce a physically sound model. Note that STO's cubic phase does not present any purely elastic instability [13], and the harmonic elastic energy is thus bounded from below. As regards the strain-phonon coupling energy, we restrict ourselves to the lowest-order terms allowed by symmetry, which are quadratic in the displacements and linear in the strains.

We split the interatomic interactions in two parts, short-range (chemical) and long-range (Coulombic), the latter being amenable to analytical treatment. More precisely, we treated the long-range electrostatic couplings exactly as in Ref. [13]: We used the well-known analytical formula for the harmonic coupling between electric dipoles, which ultimately depends only on the atomic Born charge tensors and the high-frequency (purely electronic) dielectric response of the material [17]. As regards the short-range harmonic interactions, previous investigations on the phonon band structure of the cubic phase of STO [13] and similar compounds [44] show that they decay quickly with distance, and that a $2 \times 2 \times 2$ repetition of the elemental 5-atom cell is enough to capture all the significant ones. As regards the short-range anharmonic interactions, previous modeling works [13] indicate that they are even shorter in range. (They are treated as on-site or self-energy terms in most models in the literature [36, 42, 45, 46].)

Hence, we consider all the terms within the interaction range defined by the $2 \times 2 \times 2$ 40-atom supercell. We allow anharmonic interactions to extend as far as the short-range harmonic ones, i.e., up to the maximum distance effectively defined by our 40-atom supercell. Finally, we allow all our coupling terms to involve as many atoms (bodies) as their order allows.

We then generate all the symmetry-allowed polynomial terms compatible with these cutoffs. For E_p we obtain 45 harmonic terms, 79 3rd-order ones, and 275 4th-order ones; for E_s we obtain 3 terms, and 161 terms for E_{sp} . Note that these terms only depend on the structure and symmetry of the ideal cubic perovskite phase; hence, they can be applied to the study of any such material, not only

STO.

In the following we present various exercises aimed at exploring our new recipe to fit the lattice potentials thus defined from a TS of DFT data. Yet, two parts of these potentials (the bare elastic energy and the dipole-dipole interactions, both truncated at the harmonic level) can be trivially obtained from perturbational [17, 47] or finite-difference DFT simulations. Further, these two parts of the energy are very simple, and would not benefit from any additional optimization provided by our systematic fitting procedure. Hence, for these terms we use the values directly obtained from DFT and given in Appendix B; they are thus included in E^{fixed} [Eq. (8)] in the fits.

C. Preliminary test: exact harmonic potential

The harmonic part of our model describes the PES around the RS, i.e., the interatomic couplings determining the phonon spectrum of the cubic phase. The phonon spectrum of a given structure can be computed from first principles via perturbative [17] or finite-displacement methods that give access to the interactions in real space. Hence, it should be relatively easy for us to construct models of the type proposed here and having an essentially exact harmonic part; note that the construction approach described in Ref. 13 took advantage of this fact.

However, the present scheme focuses on fitting, as opposed to explicitly computing, the model parameters to produce potentials of optimal complexity and size. Further, here we work with a Taylor series written in terms of products of displacement differences, the harmonic part of our potential having the form

$$E_p^{\text{har}}(\mathbf{u}) = \frac{1}{2} \sum_{\substack{ijkh \\ \alpha\beta}} \tilde{K}_{ij\alpha kh\beta}^{(2)} (u_{i\alpha} - u_{j\alpha})(u_{k\beta} - u_{h\beta}), \quad (19)$$

in contrast with the usual expression in terms of products of simple displacements

$$E_p^{\text{har}}(\mathbf{u}) = \frac{1}{2} \sum_{\substack{ijkh \\ \alpha\beta}} K_{ij\alpha\beta}^{(2)} u_{i\alpha} u_{j\beta}, \quad (20)$$

which is commonly used in phonon analysis. Hence, it is worth testing our present scheme by applying it to obtain the harmonic part of the PES around the RS, to explicitly confirm whether our fitting procedure and displacement-difference representation are able to yield an essentially perfect description.

To do this, we use a TS composed of the following structures: the LDA-relaxed cubic phase of STO in a $2 \times 2 \times 2$ supercell (our RS) and slightly distorted versions of the RS in which we move individual atoms by 0.015 Å. (These are exactly the same structures one would consider to compute the phonons of STO's cubic phase by the finite-displacements method.) Then, we run the fitting procedure described in Section II, considering a set

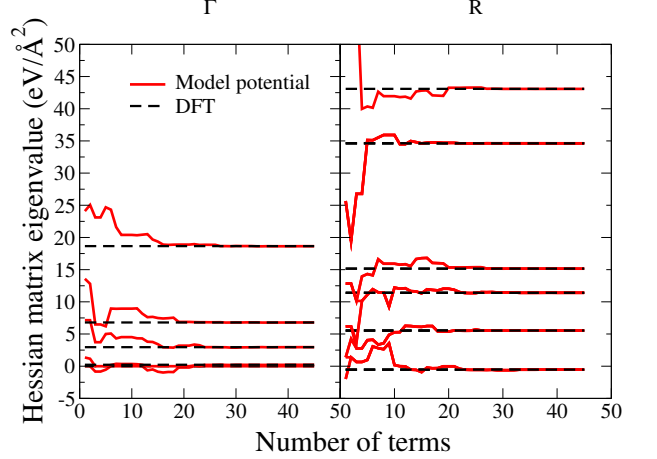


FIG. 3. Eigenvalues obtained from the diagonalization of the harmonic part of the phonon energy E_p , at two specific q -points Γ and R (see text). The solid lines indicate the results obtained from the fitted model as a function of the number of terms included, while the exact DFT-computed results are given by dashed lines.

$\mathcal{T}_p^{\text{har}}$ that includes all the possible (45) short-range harmonic terms compatible with the cutoffs described above. As mentioned above, the harmonic dipole-dipole interactions are computed analytically and included in E^{fixed} .

To present our results, let us recall that the harmonic part of the energy can be expressed in a more compact form if we use the basis of eigenvectors of the force-constant matrix $\mathbf{K}^{(2)}$. Thus, given a model of p harmonic terms $\mathcal{T}_p^{\text{har}}$, we can expand the displacement-difference products to obtain the corresponding force-constant matrix $\mathbf{K}^{(2)}[\Theta]$, diagonalize it, and compare the results with the exact LDA solution.

Figure 3 shows the results as a function of the number of terms in the harmonic model; in particular, we show the eigenvalues corresponding to q -points Γ [$\mathbf{q}_\Gamma = (0, 0, 0)$] and R [$\mathbf{q}_R = 2\pi/a(1/2, 1/2, 1/2)$, where a is the lattice constant of the 5-atom RS cell]. As we can see, the agreement is essentially perfect for p -models with $p \gtrsim 30$, confirming that our scheme is able to produce exact harmonic models *and*, in passing, automatically identify the dominant interactions. In Section III F we will briefly discuss the most important of such couplings.

D. Choice of training sets, targeted models

We generate several TSs aimed at exploring the configuration space accessible at various temperatures. More precisely, we generate TSs at 10 K and 300 K; additionally, we compute test sets at 200 K and 500 K. Our training and test sets are obtained from MD runs employing a 40-atom ($2 \times 2 \times 2$) STO supercell, which, as argued above, we deem sufficient to obtain information about the rele-

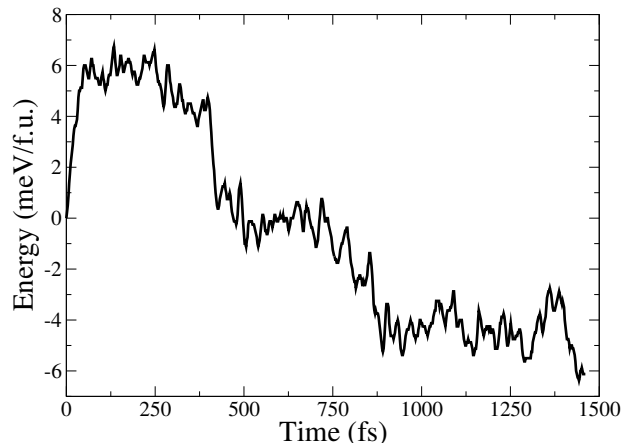


FIG. 4. Energy evolution as a function of time corresponding to the typical MD run used to construct our TSs of DFT data. This particular case corresponds to the run used to build TS@10 (see text). The run starts from the RS, which is taken to be the zero of energy. Eventually the simulated system finds its way to the ground state structure and fluctuates around it.

vant short-range interactions. Further, the MD runs are performed at 0 GPa, allowing the cell volume and shape to fluctuate during the simulation; this permits access to information concerning the strain-dependent parts of the potential.

Note that, strictly speaking, our small 40-atom simulation supercell does not allow us to talk about a well defined temperature in our MD runs; our target temperature is just a convenient handle that we use to push the system into exploring different regions of configuration space.

We find it important to start all our MD runs from the RS, for the following reason. As shown in Fig. 4, the length of our typical MD run is about 1500 fs, including an initial stage in which the system explores the surroundings of the cubic phase (the potential energy increases considerably as the atoms move following the random initial velocities compatible with a 10 K kinetic energy) to eventually (at about 400 fs in the figure) start moving towards the ground state. Once a MD run is computed, we construct the corresponding TS by picking 100 configurations from the trajectory; we pick such configurations randomly, but making sure they are homogeneously distributed throughout the MD trajectory, so as to retain information on the initial part of the run. This is necessary to obtain models that yield accurate energy differences. Indeed, because our scheme is based on fitting energy derivatives, in order to get an accurate energy difference between two structures (e.g., and most importantly, between the RS and the ground state), we need the model to describe well the connecting path.

Here we discuss models constructed by fitting to three

TABLE I. List of the STO models constructed in this work (see text). The number of parameters in the optimum cross-validated models is indicated in the last column. For the EHM, we also indicate that we retain 45 harmonic terms in E_p , i.e., all the independent interactions within our $2 \times 2 \times 2$ supercell.

Number	Fit type	TS	Parameters retained
1	FM	TS@10	33
2	EHM	TS@10	45+10
3	FM	TS@300	37
4	EHM	TS@300	45+14
5	FM	TS@10+300	44
6	EHM	TS@10+300	45+17

different TSs, one obtained from a MD run at 10 K (denoted “TS@10” in the following), a second one obtained from a MD run at 300 K (“TS@300”), and a third one that combines configurations from TS@10 and TS@300 (“TS@10+300”). The TS@10 explores the low-energy configurations of the material, and contains the kind of information that has been traditionally included in effective models of STO and similar compounds [32, 36, 41–43]. *A priori* we do not expect the models obtained from TS@10 to accurately describe the configuration space that the material explores at higher temperatures; hence the interest in considering TS@300 as well. Finally, we consider TS@10+300 to investigate the possibility of creating models that give a good description of low- and high-energy configurations simultaneously.

As we will see below, obtaining an accurate description of the low-energy PES of STO is not an easy task. In particular, we find it critical to complement the TSs with a single additional configuration that competes in energy with the ground state but is not visited in our default MD runs. Such a low-energy state is denoted $a^0a^0c^+$ in Glazer’s notation; it involves in-phase rotations of the O_6 octahedra about one of the principal axes of the perovskite lattice (recall that the rotations are in antiphase in STO’s ground state). Hence, our TS@10 and TS@10+300 training sets are completed with this additional piece of information.

Finally, as shown in Section III C, it is possible to compute the harmonic part of the model in an essentially exact way. Hence, here we discuss models in which we fit all the short-range phonon and strain-phonon couplings freely (“free models” or FMs in the following) and also models in which the exact harmonic part of E_p is retained in E^{fixed} (“exact harmonic models” or EHM in the following). This allows us to test the importance (and evaluate the convenience) of having a perfect description of the harmonic energy around the the RS.

Table I lists the six models that we discuss below, indicating the short labels we use to denote them.

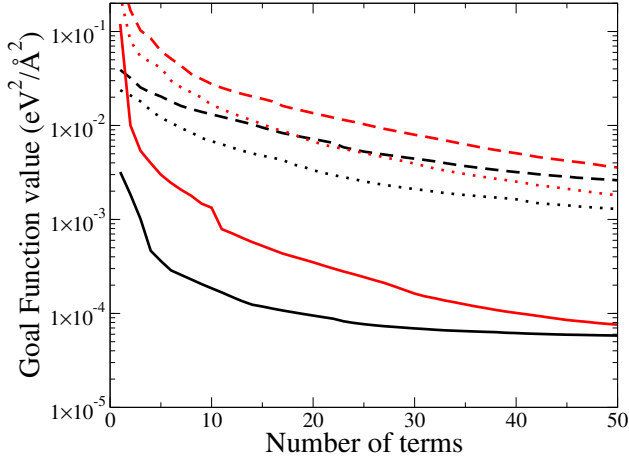


FIG. 5. Optimized goal function, as a function of the number of terms, for the various models considered in this work. Red and black lines correspond to FM and EHM models, respectively. Solid, dashed, and dotted lines correspond to models fitted to the TS@10, TS@300, and TS@10+300, respectively. See text for details.

E. Finding optimum models

Given a TS and a pool of possible parameters, the fitting procedure described in Section II is automatic. Yet, one critical issue remains, namely, how to determine the optimal size of a model. The search for optimum models comprises two aspects. At a practical level, we want to identify the simplest (smallest) models that are computationally light and, at the same time, reproduce the TS data accurately enough. At a more basic level, we want to produce models that are predictive, i.e., that do not suffer from *overfitting*. To achieve this latter goal, we must implement a cross-validation procedure, which will be the focus of the following discussion.

1. Classic cross-validation

Figure 5 shows the evolution of the goal function G , as a function of the number of terms in the model, for each of the six cases in Table I. In all cases the GF evolves rather smoothly and converges, in the limit of a large number of parameters, to values in the range between 10^{-4} eV²/Å² and 10^{-2} eV²/Å². At convergence, the lowest GF values correspond to the two models fitted to TS@10, while the largest ones correspond to the two TS@300 potentials. This indicates that it is harder to get accurate fits of MD data obtained at higher temperatures. (Since the higher-temperature TSs involve larger distortions of the RS, we should be able to improve the accuracy of the TS@300 and TS@10+300 models by increasing the maximum order of our polynomial potential.) Finally, Fig. 5 shows that, for a given TS and same number of fitted

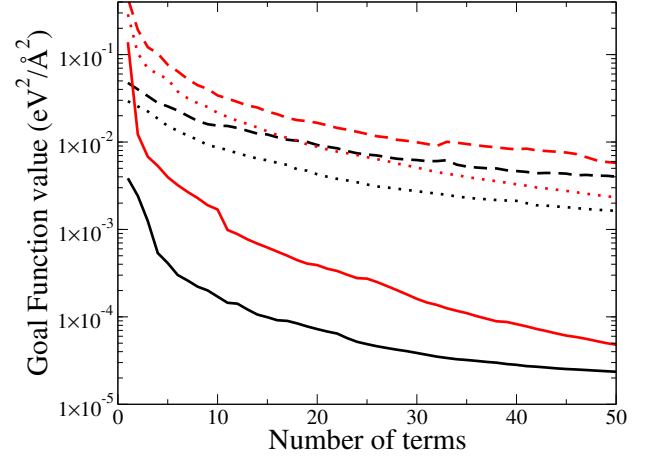


FIG. 6. Behavior of the goal function evaluated using fitted models and test-set configurations, as described in the text. The colors and line types are as in Fig. 5.

parameters, the exact harmonic models are always more accurate than the free models. This was to be expected, as EHM fits start from a nearly perfect description of the energetics of small distortions (involving 45 harmonic parameters fitted as in Section III C), while the FM fits start from scratch. As suggested by the results in Fig. 5, the EHM and FM curves corresponding to a particular TS tend to merge in the limit of very large models.

As the models increase in size, the fits rely more and more on details of the TS data that may not relate to the basic lattice-dynamical behavior of the material; instead, they may be the result of small intricate features of the interaction potential, or even be caused by numerical inaccuracy in the DFT simulations. Models incorporating that kind of information will loose in predictive power, an undesired effect that is usually known as *overfitting*. As a first attempt to determine the optimum size of a predictive model, we apply the cross-validation procedure described in Section II C – i.e., the leave- n -out method –, which we slightly modify for convenience.

To explain how we proceed, let us consider the representative case of the FMs fitted to TS@10. We take the family of FMs fitted to the complete TS@10, whose corresponding GF curve is shown in Fig. 5, as our models to cross-validate. Then, we resort to the MD run from which we obtain TS@10, and simply select a different collection of 50 configurations to construct a test set that is qualitatively similar to TS@10. Then, we evaluate the GF by using the FM parameters fitted to TS@10 *but* summing over the configurations in the test set. The results for the GF thus evaluated, as a function of the number of parameters in the model, are shown in Fig. 6 for all six models in Table I. Notably, the obtained curves are qualitatively (and quantitatively) similar to those of Fig. 5, which were obtained from actual GF minimizations. (For the TS@10 models, the GF curves in Fig. 6

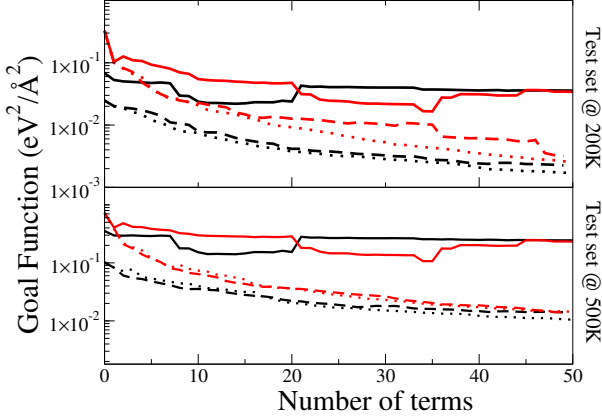


FIG. 7. Behavior of the goal function evaluated using fitted models and test-set configurations, as described in the text. The colors and line types are as in Fig. 5.

are lower than those in Fig. 5, which we have checked is a coincidence related to our selecting – randomly – a relatively *benign* test set.) Most importantly, the GF curves in Fig. 6 decrease monotonically, i.e., they do not display any minimum and do not allow us to determine an optimum model size [21]. Further analysis suggest that this *failure* is related to the fact that our TSs are quite complete and, hence, the leave- n -out method is not testing the predictive power of the corresponding models in any significant way. Noting that, in general, we will be able to afford (and want to work with) exhaustive TSs as the ones considered here, the leave- n -out cross-validation method seems inadequate for our purposes.

2. Alternative cross-validation criteria

We then try to validate our models against DFT data that are qualitatively different from those used to construct them. Our first experiment is to use test sets obtained from MD trajectories thermalized to two temperatures (namely, 200 K and 500 K) that deviate significantly from those of our reference TSs (i.e., 10 K and 300 K). The results for the GFs evaluated against such test sets are shown in Fig. 7. Most interestingly, the curves corresponding to the TS@10 models are not trivial in this case: they present one or more minima, which could provide us with a criterion to select optimum predictive potentials. It is worth noting that, when we test the TS@10 models against 500 K data, such minima correspond to a relatively small number of parameters; in contrast, the minima occur for relatively large models when we use the test set obtained at 200 K. This reflects the fact that the TS@10 models become less accurate for the description of larger RS distortions, as those corresponding to MD trajectories obtained at higher temper-

atures; accordingly, the cross-validation procedure suggest that simpler TS@10-fitted potentials will do a better job at capturing the general features of typical high-temperature configurations of the material.

Figure 7 also shows that the GF values for the TS@10 models are relatively large; in contrast, those for the TS@10+300 and TS@300 models are quite small, and approach those in Fig. 5 obtained from an explicit GF optimization. This shows that the TS@10+300 and TS@300 models excel at describing the configurations associated to the 200 K and 500 K MD trajectories. (Actually, even the performance of the TS@10 model is much better than it may seem from Fig. 7, as we will see below.) Accordingly, these test sets are not challenging the predictive power of such models, and the corresponding GF curves are monotonically decreasing. Hence, this cross-validation strategy is not fully satisfactory either.

Finally, we try to cross-validate our models by checking their predictions for several key structural and energetic features of the PES of STO. In particular, for materials like STO, which undergoes a structural phase transition driven by a soft phonon mode, it has been shown [48, 49] that the transition temperature correlates strongly with the energy difference between the high- and low-symmetry phases (which are, in our case, the cubic RS and the tetragonal ground state, respectively) and the amplitude of the corresponding structural distortion (for STO, this is best quantified by the rotation angle of the O_6 octahedra). Figure 8 thus shows what our models predict for these critical quantities, as a function of the number of parameters. The figure also shows how well each particular model reproduces the energetics of the MD trajectory used to construct the TS to which the model was fitted (thus, e.g., the TS@10 models are tested against the MD trajectory obtained at 10 K). Finally, Fig. 8 shows how well our models reproduce the energetics of the DFT-computed MD trajectories at 200 K and 500 K. Note that our interest in using energy differences to test our models is two-fold: On one hand, the energy is the critical quantity that will determine the equilibrium properties of our materials of interest as a function of temperature, as obtained e.g. from Monte Carlo simulations. On the other hand, we do not (explicitly) use energies to calculate the model parameters; hence, checking the energies computed with our potentials implies a test of their predictive power, even if we restrict ourselves to the configurations in the TSs used for the fits.

The results shown in Fig. 8 can be viewed from two different angles. On one hand, they are somewhat disappointing as a cross-validation exercise. For example, it could be argued from these results that the performance of the TS@10 and TS@300 models tends to deteriorate, for an increasing number of terms, when it comes to describe the 500 K [e.g. panel (i)] and ground state [e.g. panel (c)] data, respectively. However, it is all but impossible to identify an optimum model size from the erratic-looking curves that we obtain. Further, in the TS@10+300 cases, the performance improves rather con-

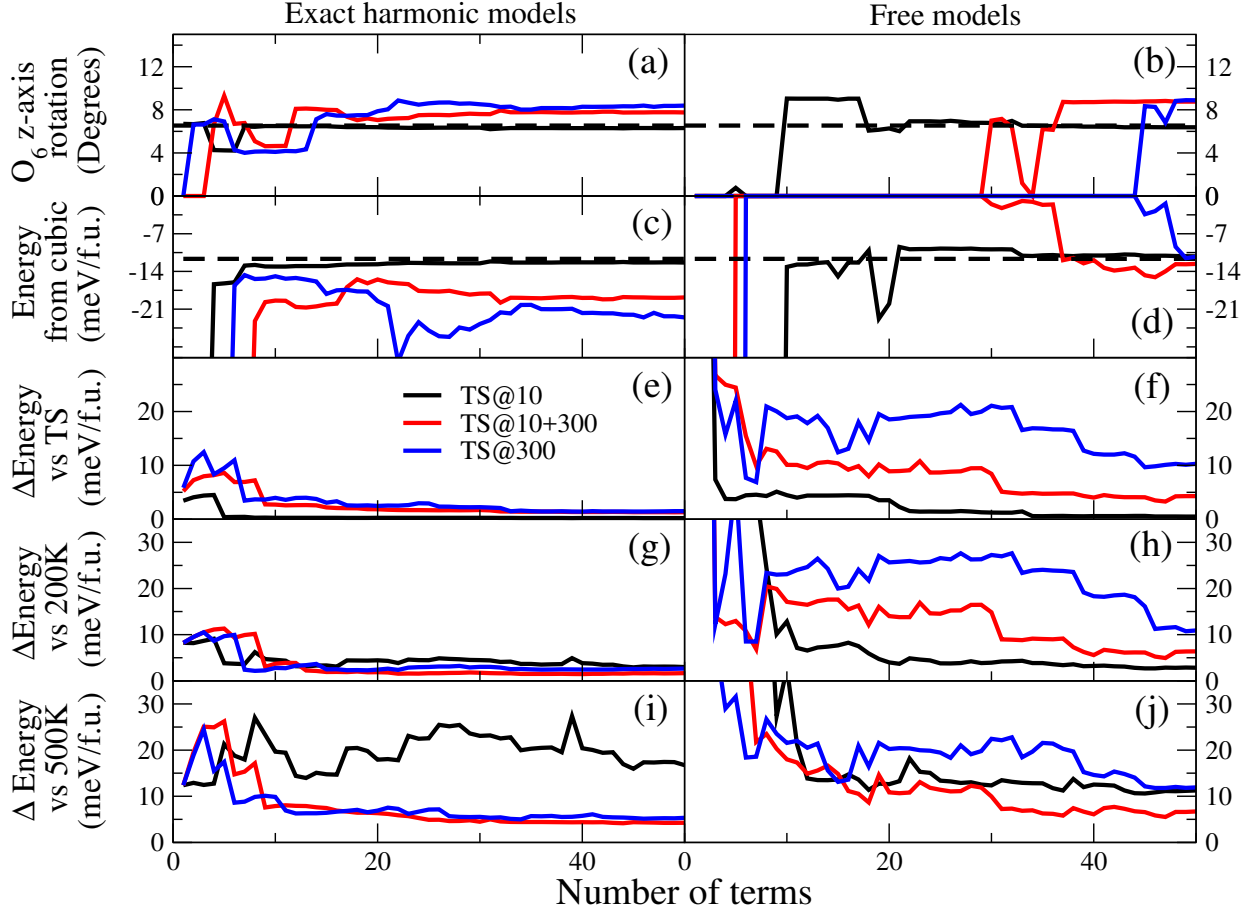


FIG. 8. Performance of the six models discussed in this work as regards the prediction of various ground state [panels (a-d)] and MD [panels (e-j)] related quantities. To obtain the data in panels (e-j), we use our model potentials to compute the energy of the configurations visited in the MD trajectories computed from DFT at various temperatures; we report the average difference between the DFT energy and that obtained from the model.

tinuously, for all the considered quantities, as the models grow; in other words, our new set of tests is not challenging sufficiently the predictive power of the TS@10+300 models.

On the other hand, the results in Fig. 8 provide a very convenient quantitative test of the quality of the models; a test that is far more useful than the GF results in Figs. 5, 6 and 7, whose significance is difficult to judge. For example, Fig. 8 reveals that the TS@10+300 and TS@300 models have great difficulties to capture the energy difference between RS and ground state with acceptable precision, despite the great quantitative accuracy suggested by the previous GF-based criteria. (Indeed, note that the FMs for TS@300 and TS@10+300 predict the correct ground state only after a rather large number of terms have been included.) In contrast, the data in Fig. 8 shows that the TS@10 models perform incredibly well to predict the energy of the configurations that are typical of the 200 K MD trajectory (average deviations being below a tiny 5 meV/f.u.), and give acceptable re-

sults (with deviations between 10 and 20 meV/f.u.) for the 500 K structures. Hence, while the TS@10 models may have seemed quite crude according to the GF results of Fig. 7, the data in Fig. 8 indicates that they may constitute the most reasonable choice among all the options we have investigated.

In conclusion, Fig. 8 provides us with the criteria that we find most convincing to determine the optimum size of our models. The results in the figure allow us to quantify the accuracy of the potentials according to a set of demanding tests that are directly linked to the properties that will be most relevant for future statistical and dynamical simulations. Hence, we think they provide us a sufficient information to determine the minimal models that are both predictive and sufficiently accurate.

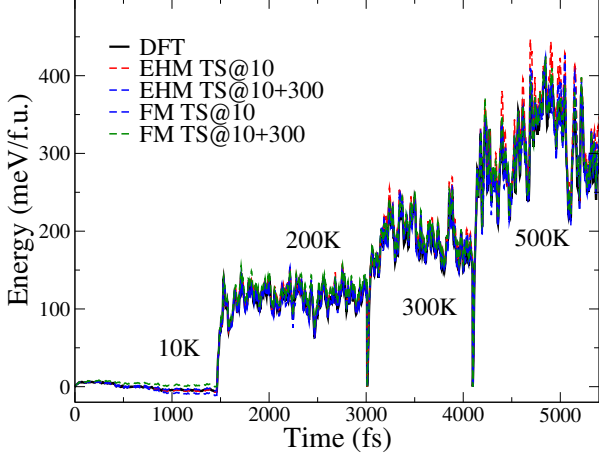


FIG. 9. Comparison of the DFT-computed energy for MD trajectories at various temperatures and the energies obtained by evaluating our optimum model potentials for the corresponding structures. Except in the 10 K and 500 K cases, the deviations in the energy are all but invisible in the scale of the figure, emphasizing the good overall accuracy of our fitted models.

3. Optimum models

By inspection of Fig. 8, we decided the optimum size of the six models of interest here. The number of parameters finally chosen for each of the models is indicated in Table I. Figure 9 shows how well the models reproduce the energy of the configurations in our DFT-computed MD trajectories, evidencing the great overall agreement. Note that the energy deviations for a trajectory at a given temperature are minute when compared with the energy difference between trajectories at different temperatures; note also that it is the latter energy scale that is expected to govern the most notorious dynamic and thermodynamic properties of the material, in particular its structural transformations. Table II gives additional quantitative details on the performance of the TS@10 and TS@10+300 models. Note that we have not included the results for the models fitted to TS@300 here, as their poor results for STO's ground state properties discourages further consideration of such potentials.

F. Analysis of the optimum models, interactions

We now comment on the models produced by our fitting procedure, which automatically selects the most relevant interactions out of a pool that virtually includes all possible ones. (Note that we retain an average of 38 terms in our optimum FM models, out of over 550 possible ones.) Here we focus on the general aspects that pertain to our potential-construction approach, touching only briefly on the particular physics of STO.

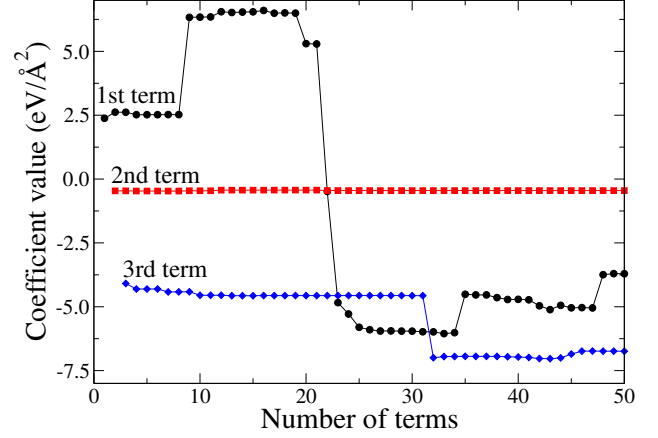


FIG. 10. Values of the three parameters that our fitting procedure selects as most relevant to construct the EHM fitted to TS@10. The figure shows their evolution as a function of the total number of terms included in the model. Note that all three terms are linear in strain and quadratic in the atomic distortions; hence, they all have the same units, as indicated in the figure.

Our model fitting procedure is essentially a black box, and one may wonder about the actual physical significance of the specific interactions and parameter values associated to a specific best p -model. Note that, as we consider increasingly complex models \mathcal{T}_{p+1} with $p+1$ terms, all the p parameters in the simpler model $\mathcal{T}_p^* \subset \mathcal{T}_{p+1}$ are refitted, and their values will inevitably change. Hence, the actual value of a specific interaction depends on the number of terms in the model, which raises the question of how significant such a value actually is. The situation is illustrated in Fig. 10, which shows the evolution of the three most important terms that are automatically identified when constructing the EHM fitted to TS@10; the specific couplings associated to such parameters are indicated in Table III. As we can see, the second most important parameter remains nearly constant as we increase the number of interactions in the model. In contrast, the first and third most important parameters display drastic changes in their fitted value; in fact, the interaction determined to be most critical, which describes the way in which cell strains control the interactions between nearest-neighboring oxygens (see Table III), even changes sign as the model goes above 22 terms, and does not seem to converge to a steady value even for rather complete models.

Interestingly, the most significant changes in the values of the first and third parameters in Fig. 10 occur rather abruptly, and coincide with the inclusion of very specific interaction terms in the best p -model. The details are summarized in Table III. We can see that, for example, the discontinuities in the value of the first parameter (number 1 in Table III) correspond to the inclusion of

TABLE II. Properties characterizing the behavior of the optimum models that we consider for MC simulations. Values obtained with the original optimum models are given; we also give in parenthesis the values computed using the energy-bounded models. In the last row, ΔE is the average energy difference, for the configurations included in the corresponding TS, between the LDA results and the energies evaluated with our potentials.

	FM TS@10	EHM TS@10	FM TS@10+300	EHM TS@10+300	LDA
O ₆ rotation (degrees)	6.5 (6.5)	6.5 (6.5)	9.9 (8.7)	8.3 (8.1)	6.5
Ground state energy (meV/f.u.)	-11.1 (-11.1)	-13.2 (-13.1)	-13.2 (-11.9)	-22.9 (-20.7)	-11.7
Goal function ($\text{eV}^2 \text{\AA}^{-2} \times 10^{-3}$)	0.14 (0.14)	0.18 (0.19)	2.79 (2.81)	4.94 (5.40)	
ΔE (meV/f.u.)	0.58 (1.45)	0.30 (0.27)	4.74 (4.78)	2.31 (2.57)	

TABLE III. Each row corresponds to one of the three parameters identified to be the most relevant ones for the EHM model fitted to TS@10, indicated by #1, #2, and #3, respectively. We indicate the corresponding interaction (in the notation of Appendix B) and, in parenthesis, the value of the GF corresponding to the best 1-model, 2-model, and 3-model, respectively. Further, we indicate the terms that are related with these most important ones and whose inclusion in the model causes the discontinuities in their values shown in Fig. 10. Thus, for parameter #1, we also include parameters #9 and #22. In such cases, we give in parenthesis the value of the GF that corresponds to considering a best 1-model composed of parameter #9 or #22; note that these values are very close to the minimum GF obtained for parameter #1. All GF values are given in $\text{eV}^2 \text{\AA}^{-2}$.

#1: $\eta_2(\text{O1}_x - \text{O2}_x)(\text{O1}_y - \text{O2}_y)$ (0.00320)	#9: $\eta_1(\text{Ti}_x - \text{O3}_x)^2$ (0.00328)	#22: $\eta_3(\text{O2}_y - \text{O3}_y)^2$ (0.00324)
#2: $\eta_1(\text{O2}_z - \text{O3}_z)^2$ (0.00185)		
#3: $\eta_4(\text{Sr}_z - \text{O1}_z)(\text{Sr}_y - \text{O1}_y)$ (0.00101)	#32: $\eta_4(\text{O1}_y - \text{O3}_y)(\text{O1}_x - \text{O3}_x)$ (0.00102)	

additional strain-phonon couplings (numbers 9 and 22 in the same table) that bear obvious similarities with the interaction chosen to be most relevant; naturally, these couplings are connected to the same kind of interatomic forces and cell stresses in our TS data, and their computed values are strongly dependent on whether or not we include all of them in the fit. In other words, the parameter values computed for the simpler models effectively account for the additional interactions that are not included, which can be viewed as a renormalization of sorts. Table 10 also gives the values of the GF that determined the selection of a given interaction term instead of the related ones; thus, for example, when finding the best 3-model, the parameter picked as number 3 got a GF score of $0.00101 \text{ eV}^2/\text{\AA}^2$, while the parameter eventually picked as number 32 got $0.00102 \text{ eV}^2/\text{\AA}^2$. Hence, we find that related interaction terms tend to render similarly good fits, and retaining one of them instead of the competing ones may well be a matter of the details of our TS.

These observations clearly suggest that we should be cautious and avoid overinterpreting the physical relevance of the particular interaction terms retained in our optimum models, especially in the case of relatively simple potentials. Obviously, there is physical information in the couplings automatically identified to be most relevant (more on this below); however, the specifics depend strongly on the size of the model and, presumably, the details of the TS.

Let us now turn to aspects that are more specifically related to our subject case, STO, focusing on two essential and non-technical issues. First, when defining our pool of potential interactions in Section IIIB, we assumed that our short-range harmonic couplings, and all anharmonic

ones, decay quickly with the interatomic distance. Figure 11 shows representative results confirming that such a fast decrease in the magnitude of the interactions is observed in our fitted models, clearly supporting our initial hypothesis. Indeed, we find that our optimum models – which we determine based on validation criteria that are oblivious of the nature of the underlying couplings – turn out to be very short-ranged; as can be seen in Fig. 11, all the retained interactions are within a 5.5 \AA range.

Second, Fig. 12 and Table IV give some detail about the interactions that our scheme determines to be most relevant to fit the TS data. The first thing to note is that we see many coincidences among the interaction terms retained in models fitted to different TSs (TS@10 and TS@10+300) and irrespective of the way in which the harmonic part of E_p is treated. Another notable fact is that the majority of terms found to be most important are *active* as regards (i.e., they contribute to the energetics of) the two most relevant structural distortions of the STO lattice, namely, the AFD O₆-rotational instabilities of the cubic phase that lead to the low-temperature ferroelastic structure and the low-energy polar distortions (mostly characterized by the stretching of the Ti–O bonds) that control the dielectric response. Finally, the strain-phonon coupling terms always occupy preeminent positions in the importance-ordered list provided by our automatic fit, reflecting the known sensitivity of STO’s AFD and polar phonons to strain deformations.

G. Energy boundedness

As mentioned in Section IID, the polynomial models we obtain by default are likely to be unbounded from

TABLE IV. List of most important interactions, as selected by our automatic fitting procedure, for our FM and EHM models fitted to TS@10 and TS@10+300. The harmonic part of E_p is common to both EHM models. The numbers indicate the order in which the interactions appeared in the corresponding automatic selection process. We include the leading interactions for the different parts of the energy in our potentials. The interactions are specified following the notation of Appendix B. We indicate with an asterisk the couplings depicted pictorially in Fig. 12.

Free models	
TS@10	TS@10+300
Harmonic part of E_p	
1*: $(\text{Ti}_y - \text{O}_{2y})^2$	1*: $(\text{Ti}_y - \text{O}_{2y})^2$
2*: $(\text{O}_{3y} - \text{Ti}_y[010])(\text{Ti}_y - \text{O}_{3y})$	2*: $(\text{O}_{3y} - \text{Ti}_y[010])(\text{Ti}_y - \text{O}_{3y})$
6: $(\text{Sr}_x - \text{O}_{1x})(\text{Sr}_z - \text{O}_{3z})$	4: $(\text{Sr}_x - \text{O}_{1x})(\text{Sr}_z - \text{O}_{3z})$
Anharmonic part of E_p	
13: $(\text{Sr}_x - \text{O}_{2x})^2(\text{Sr}_z - \text{O}_{3z})$	8: $(\text{Ti}_y - \text{O}_{2y})^3$
14: $(\text{Ti}_z[010] - \text{O}_{2z}[010])(\text{Ti}_z - \text{O}_{2z}[010])(\text{Ti}_y - \text{O}_{2y}[010])$	14: $(\text{Ti}_z[010] - \text{O}_{2z}[010])(\text{Ti}_z - \text{O}_{2z}[010])(\text{Ti}_y - \text{O}_{2y}[010])$
18: $(\text{Sr}_x - \text{O}_{2x})^2(\text{O}_{2x} - \text{Sr}_x[001])^2$	16: $(\text{Sr}_z - \text{O}_{1z})(\text{Sr}_y - \text{O}_{1y})^2$
Strain-phonon coupling E_{sp}	
3*: $\eta_2(\text{O}_{1x} - \text{O}_{2x})(\text{O}_{1y} - \text{O}_{2y})$	3*: $\eta_3(\text{Ti}_z - \text{O}_{3z})^2$
4*: $\eta_2(\text{Sr}_x - \text{O}_{3x})^2$	9*: $\eta_2(\text{O}_{1x} - \text{O}_{2x})(\text{O}_{1y} - \text{O}_{2y})$
5: $\eta_6(\text{Sr}_y - \text{O}_{3y}[001])(\text{Sr}_x - \text{O}_{3x}[001])$	10*: $\eta_2(\text{Sr}_x - \text{O}_{3x})^2$
Exact harmonic models	
Harmonic part of E_p	
1*: $(\text{Ti}_y - \text{O}_{2y})^2$	
2*: $(\text{Ti}_x - \text{O}_{2x})(\text{Ti}_x - \text{O}_{1x})$	
3*: $(\text{O}_{3y} - \text{Ti}_y[010])(\text{Ti}_y - \text{O}_{3y})$	
TS@10	TS@10+300
Anharmonic part of E_p	
4: $(\text{Ti}_x - \text{O}_{2x})^2(\text{O}_{1y} - \text{O}_{3y})^2$	2: $(\text{Ti}_y - \text{O}_{2y})^3$
5: $(\text{Ti}_z[010] - \text{O}_{2z}[010])(\text{Ti}_z - \text{O}_{2z}[010])(\text{Ti}_y - \text{O}_{2y}[010])$	5: $(\text{Ti}_z - \text{O}_{1z})(\text{Ti}_z - \text{O}_{3z}[001])^2(\text{Ti}_z - \text{O}_{3z})$
6: $(\text{Sr}_x - \text{O}_{2x})^2(\text{Sr}_z - \text{O}_{3z})$	7: $(\text{Ti}_z[010] - \text{O}_{2z}[010])(\text{Ti}_z - \text{O}_{2z}[010])(\text{Ti}_y - \text{O}_{2y}[010])$
Strain-phonon coupling E_{sp}	
1*: $\eta_2(\text{O}_{1x} - \text{O}_{2x})(\text{O}_{1y} - \text{O}_{2y})$	1*: $\eta_3(\text{Ti}_z - \text{O}_{3z})^2$
2: $\eta_1(\text{O}_{2z} - \text{O}_{3z}[100])^2$	3*: $\eta_2(\text{Sr}_x - \text{O}_{3x})^2$
3*: $\eta_4(\text{Sr}_z - \text{O}_{1z})(\text{Sr}_y - \text{O}_{1y})$	4: $\eta_1(\text{O}_{3y} - \text{O}_{1y}[010])^2$

below, as there is nothing in our fitting procedure that controls the behavior of the energy for very large distortions of the RS. In the course of this work we have tried a number of strategies to tackle this problem, most of which were not easy to implement in an automatic way, or led to models with a significantly reduced accuracy. Here we briefly describe some of those attempts, and in the end discuss the approach we found most satisfactory and finally implemented.

1. Quasi-automatic approaches

Ideally we would like to have an energy-bounding strategy that is as automatic as our model-construction procedure. Here we discuss two representative alternatives that comply with such a requirement.

One possibility is to supplement the models with a bounding potential that (1) is small (or even null) for the distortion amplitudes that are typical of our TSs and (2) overpowers our fitted potential outside that region to guarantee boundedness from below. This approach

has two distinct advantages: the resulting models are bounded by construction and their quality, as measured by the GF used to fit them, is essentially unaffected. However, it also presents some serious drawbacks, at least for a material as demanding as STO: The models thus bounded suffer from a drastic loss of predictive power for configurations not contained in the TS (in particular, the highly desirable matching of energy scales for MD trajectories at different temperatures, which is shown in Fig. 9, is all but lost) and tend to display spurious local minima of the energy that compromise the results of statistical simulations. Unfortunately, fighting against the latter problem tends to exacerbate the former, which led us to disregard this approach.

A second possibility is to identify, and remove from the pool of possible interactions, the terms that cause the energy unboundedness. While this approach may seem rather drastic, it is partly justified by the observation (see Section III F) that there is some degree of arbitrariness in what regards the coupling terms selected as most relevant by our automatic procedure, since some of them could be replaced by similar ones without any

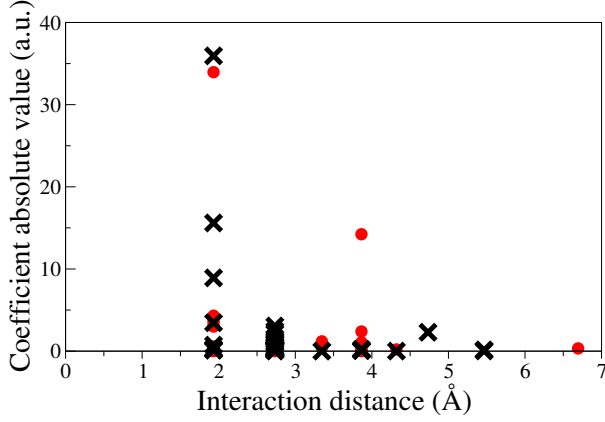


FIG. 11. Values of the parameters obtained for our FM fitted to TS@10 and ordered as a function of the longest interatomic separation associated to the corresponding coupling. The black crosses correspond to the parameters finally retained in the optimum model (i.e., to those selected as most relevant by our automatic fitting procedure), while we show the coefficients corresponding to the disregarded terms with red circles. Representative pairs of interacting atoms are indicated in the horizontal axis, following the notation in Appendix B. Note that this figure includes information about coefficients corresponding to different orders of our Taylor series, which thus have different units; hence, we indicate arbitrary units (a.u.) and stress that this figure is to be taken only as a qualitative illustration of the spatial decay of the interactions.

significant loss in the model's accuracy. We proceed as follows: We construct the best p -model in the usual way; we test it by running a set of suitable Monte Carlo annealings, which allows us to identify run-away solutions in case the model is unbounded from below; by examining the run-away trajectory, we determine the coupling term that dominates the energy divergence; we remove such a term from the pool of possible interactions and determine a new best p -model; we repeat the test until a bounded model is obtained. Interestingly, we find that in some cases such a procedure was able to deliver bounded models of excellent quality and predictive power, indicating that this may be a viable alternative when dealing with materials that are not as complex as STO. However, for some of the TSs and model-construction (FM vs. EHM) strategies considered here, the procedure does not lead to satisfactory results. Hence, we did not pursue it further in this work.

2. Practical approach

Interestingly, it is actually quite easy to identify the potentially problematic terms in our models, either automatically or by direct inspection. With this information at hand, it is typically trivial to identify a higher order

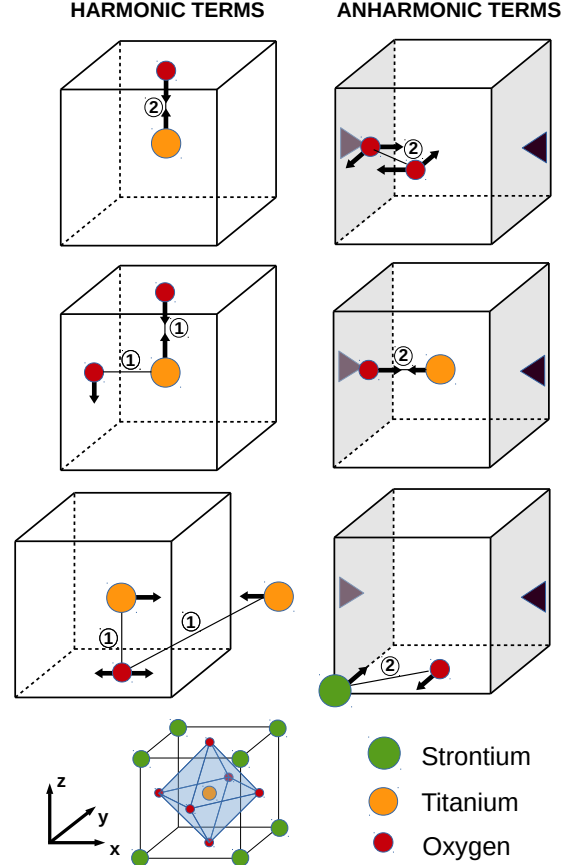


FIG. 12. Sketch of some of the most important interactions identified by our automatic fitting procedure. The atomic displacements corresponding to a representative term of the SAT are shown; strains are indicated with dark triangles. The circled numbers indicate the order of specific displacement-difference terms. Note that all the sketched interactions play a role to control the energetics of AFD modes and polar distortions, as described in the text.

coupling that can most effectively *control* the run-away solution, and thus include it to construct a well-behaved model.

For example, in the case of the FM model fitted to TS@10, our analysis shows that the optimum potential obtained by default presents run-away solutions associated with the interactions of the Ti-O pair, mainly driven by a third-order term of the form $(\text{Ti}_x\text{-O1}_x)^3$ (see term number 24 in Table A1; to describe the couplings, we adopt the compact notation used in Appendix B) as well as other more complex fourth-order terms. It is trivial to identify the sixth-order couplings [e.g. of the form $(\text{Ti}_x\text{-O1}_x)^6$] that can control the corresponding divergences. We thus extend the optimum model by adding these higher-order interactions, and refit the parameters to TS@10; in this way we compute the new high-order coupling parameters and obtain revised values for the original interactions. In the case of the FM model fit-

ted to TS@10, this procedure allowed us to obtain an energy-bounded model. (Strictly speaking, as shown in Table A1, this model also required the addition of a term of the form $\sim(\text{Sr}_x\text{O}_{1-x})^6$ to control another similar run-away solution, driven in this case by the relative Sr-O displacements.) Other cases were slightly more involved, but could be resolved by e.g. supplementing the TS with a few higher-temperature configurations (which we find tend to result in positively-defined high-order interactions that provide boundedness from below) or imposing by hand small and positive values for the parameters of (some of) the high-order terms (which we find has a minor impact on the quality of the models once the other parameters are refitted under this constraint). Importantly, the models thus bounded continue to be very accurate as regards both the GF value and the other set of validation criteria discussed in Section III E 2; see Table II for some details on the accuracy of the optimum energy-bounded potentials.

Finally, let us note that it might be possible to design an automatic implementation of this kind of correction. Let us consider an arbitrary polynomial coupling term in our potential, which we can write as $u^n v^m \dots$, where n and m are integer numbers while u and v represent any possible displacement-difference or strain factors. For any such term, it is trivial to find a related one $u^{n'} v^{m'} \dots$ where the primed exponents are defined as the smallest even number such that $n' > n$, $m' > m$, etc. If this new coupling has a positive parameter associated to it, it will obviously bound any run-away solution the original term may lead to. Hence, we can automatically identify bounding interactions for each of the couplings selected by our potential-constructions procedure; what we still lack is an automatic way to find a positive coupling parameter (by fitting to a high-temperature MD trajectory, or maybe heuristically) that results in accurate and bounded models. This development remains for future work.

H. Simulation of SrTiO₃'s structural transition

Let us now discuss the predictions that our different models yield for STO's ferroelastic phase transition. To simulate STO as a function of temperature, we run MC simulations using a periodically-repeated $12 \times 12 \times 12$ supercell that contains 8640 atoms; for temperatures close to the phase transitions, we use $16 \times 16 \times 16$ supercells (20480 atoms) to better tackle finite-size problems. Typically, the calculation at a given temperature starts from a quasi-thermalized configuration (obtained from an equilibrium simulation at a neighboring temperature), which we let evolve for 20,000 MC sweeps to fully equilibrate. This is followed by 40,000 additional sweeps to compute statistical averages. Figure 13 shows the results thus obtained for the TS@10 and TS@10+300 models; the figure shows the temperature dependence of the angle characterizing the antiphase rotations of the O₆ octahe-

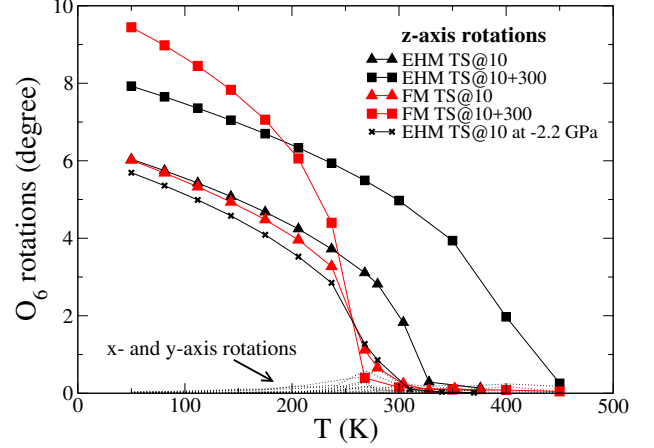


FIG. 13. Computed evolution of the AFD order parameter, as a function of temperature, for our TS@10 and TS@10+300 models. We also show the result for a pressure-corrected version of the EHM model fitted to TS@10 (see text).

dra, which is the key order parameter to study STO's transition.

As we can see, all the models yield a structural transformation in which O₆ rotations about the z axis occur. This is exactly the same transition that is observed experimentally, between the high-temperature cubic $Pm\bar{3}m$ phase and the low-temperature tetragonal $I4/mcm$ phase; hence, all our models describe the qualitative behavior of STO correctly. (In our simulations, the low-symmetry phase may present O₆ rotations about any of the principal axes in the cubic lattice; for clarity, we process our results so that the symmetry-breaking distortion is always oriented along z .)

Nevertheless, the different models lead to significant quantitative differences as regards two important features, namely, the value of the O₆ rotations in the limit of low temperatures and the transition temperature T_t . The former discrepancies were to be expected, as they directly reflect the accuracy of our models to describe the ground state structure; for example, in agreement with the data in Table II, the FM model fitted to TS@10+300 renders the largest rotation angle at low temperatures; such a value differs significantly from the smaller and nearly-identical values that result from the models fitted to TS@10, which also agree very well with the DFT result.

In contrast, the latter discrepancies on T_t were not obvious to predict *a priori* and provide us with new and important information on the behavior of our models. In essence, we find a relatively low T_t of about 270 K for the two models fitted to TS@10, as well as for the FM model fitted to TS@10+300. In contrast, the EHM model fitted to TS@10+300 results in a transition at a much higher $T_t \approx 375$ K. It is instructive to compare these findings with expectations from the literature on soft-mode driven

structural phase transitions. According to the criterion proposed in Ref. 48, which is frequently cited and followed by workers in the field, the transition temperature correlates directly with the magnitude of the structural distortion in the ground state; this rule would predict that our FM model fitted to TS10+300 should present the highest T_t among all our models, in obvious disagreement with our findings. Nevertheless, some of us [49] have recently revised the connection between transition temperatures and ground state features, concluding that the feature most directly linked to T_t is the energy difference between the ground state and the high-symmetry structure. This new rule would suggest that our EHM model fitted to TS10+300 should present the highest T_t by far, while the other three models should yield transformations at a similar temperature; this is precisely what we find, thus supporting the conclusions of Ref. 49.

Let us comment briefly on the comparison of our results with experiment. The experimental T_t of STO is known to be 110 K [50], and the O_6 rotation angle is about 2.1° at 4.2 K [50]. Our quantitative results severely overestimate these two key quantities, as we obtain values of 270 K and 6.5° , respectively, for the TS@10 models. Discrepancies of this sort, between experimental and theoretical results for STO, are not new, and it is well accepted that they must be partly related to LDA's overbinding error. Accordingly, previous first-principles models of STO have been empirically corrected by introducing an expansive external pressure [13, 32]; also, the DFT results improve significantly when other functionals are used which correct for LDA's error [51]. In our case, we tested this effect by correcting our EHM model fitted to TS@10 with an hydrostatic pressure of -2.2 GPa, which we numerically find is the largest value for which this model retains STO's experimental ($I4/mcm$) ground state (largest tensile pressures result in the stabilization of a FE distortion, an effect that is in compatible with the phase diagram in Ref. 31). The corrected model yields the results shown in Fig. 13, with a new $T_t \approx 260$ K; additionally, for such an applied pressure we obtain a O_6 -rotation angle at 0 K of about 6.2° and an energy difference between the cubic and ground state structures of about 10.9 meV/f.u. Hence, this correction improves the agreement with experiment, although not very significantly.

The remaining disagreement is not so surprising when one notes that lattice quantum effects are known to be very important in materials like STO. Such effects generally result in a reduction of transition temperatures and distortion amplitudes [32, 52], because of the additional ways to disorder (via quantum fluctuations) that they provide the material with. Hence, their inclusion in our simulations should get our results closer to the experimental values. Nevertheless, we should note that the explicit estimates made for STO [31] suggest a T_t reduction of about 15 % when including the quantum statistics, which would result in a still too high $T_t \approx 200$ K in our case. Hence, these considerations suggest that our

LDA-based models may need to be improved as regards the description of other subtle features of the PES – e.g., the competition between AFD and FE instabilities – that are known to have dramatic effects in the transition temperatures [13, 32, 53]. A detailed analysis of such issues, which would be far from trivial, remains for future work.

To conclude this section, let us note that, while the comparison with experiments on STO is far from definite, our results for the phase transition suggest several interesting conclusions. Most importantly, they indicate that our TS@10 models may be the potentials of choice for essentially any investigation of this compound. This is not a trivial observation. Note that such models focus on the description of the ground state properties and that, except for the energy difference between ground state and RS, their fit does not include any explicit information about the thermally-activated behavior of the compound. Nevertheless, they render temperature-dependent results that seem more reliable, and are closer to experiment, than those obtained from models explicitly fitted to yield a better description of higher-energy configurations (most notably, our EHM model fitted to TS@10+300).

Note also that, in order to have even better models that describe well the ground state properties (which seems mandatory) and also approach DFT accuracy for the higher-energy configurations, we should increase the order of our polynomial expansion. Indeed, from inspection of the terms retained in our models (see Figs. 11 and 12, and the discussion in Section III F), it is clear that our pool of parameters contains interactions that, in terms of both spatial range and number of bodies involved, are far more complex than what is needed to fit the TS data. At the same time, the models have obvious difficulties to account simultaneously for the PES associated to small (corresponding to TS@10) and larger (captured in TS@300) RS distortions, which suggest that the truncation at 4th order is the main limiting factor for the quality of the models constructed in this work.

IV. SUMMARY AND CONCLUSIONS

By taking advantage of a distinctive feature of the lattice-dynamical potentials recently introduced by some of us [13] – namely, the linear dependence of the energy on the free parameters of the model –, we are able to design an automatic fitting scheme that turns the calculation of the model's parameters into a simple and fast matrix diagonalization. We thus avoid the difficulties that hamper the construction of other lattice potentials, which are typically non-linear in the parameters and whose fit to a training set of data requires a numerically-costly optimization. This unique advantage, combined with the simple Taylor-series-like form of our models – which provides us with a well-defined strategy to improve them in a systematic way –, allows us to sample virtually all possible interatomic couplings during the model construction.

We can thus generate not just one model, but a family of them, of increasing complexity and accuracy in reproducing a training set of first-principles data. Then, a thorough cross-validation procedure, focused on checking our models' predictive power against the quantities that will be most critical in the simulations of specific materials (that is, in the example we discuss, the energetics and structure of the ground state, as well as the energetics of dynamical simulations at various temperatures) allows us to identify models that are simultaneously simple (thus computationally light), predictive, and accurate.

We demonstrate our scheme with an application to ferroelastic perovskite SrTiO_3 , a material that features soft mode-driven structural transitions and is a model compound for the investigation of competing lattice instabilities. Hence, this is a very demanding test case for our method, which is requested to capture subtle dynamical features that involve a highly anharmonic potential. We show that our scheme successfully allows us to rank the interatomic interactions by order of importance, revealing that the main features of the potential energy surface are controlled by couplings that are relatively short in range. This example also allows us to discuss in detail the main difficulty in our potential-construction scheme, namely, that the resulting models are not guaranteed to be bounded; we discuss several approaches to correct this problem and show that it is possible to implement a simple and practical strategy that results in bounded models with a negligible loss of accuracy. Finally, we show that our models for SrTiO_3 reproduce the basic experimental facts about the material, and briefly discuss the physics of our automatically chosen potentials.

We thus introduce a new scheme for the construction of lattice-dynamical models that approach first-principles accuracy and can be constructed in an efficient quasi-automatic way. Our scheme takes full advantage of a particular kind of potentials that have a very simple and general form. Such potentials are restricted to treat cases in which the lattice connectivity and topology is respected throughout the simulation. This constant-topology condition does not apply whenever we have formation or breaking of chemical bonds. Nevertheless, our models are an excellent choice for the investigation of a wealth of interesting physical phenomena – from the equilibrium properties of stable phases (including functional effects such as electromechanical and dielectric responses, static or dynamical), to non-reconstructive structural transitions (e.g., all those driven by soft phonon modes) or thermal (transport, electrocaloric) effects –, which underlines their interest and potential applicability. Moreover, the models can be directly used in schemes that include a description of the relevant electronic bands [5], thus mimicking an actual first-principles calculation. Hence, we are confident that our new potential-construction method will be very useful in future investigations of diverse compounds and physical phenomena.

ACKNOWLEDGMENTS

This work is funded by the Luxembourg National Research Fund through the Pearl (Grant No. FNR/P12/4853155) and AFR (Grant No. 9934186) programs. We also acknowledge support from MINECO-Spain through Grant No. MAT2013-40581-P. Some calculations were run at the CESGA supercomputing center.

Appendix A: Hessian analysis of the goal function

Following the notation introduced in Section II, the Hessian matrix associated to the equilibrium point of the goal function is

$$H_{\mu\lambda} = \frac{2}{M_1} \sum_{s\tau} \bar{f}_{\lambda\tau}(s) \bar{f}_{\mu\tau}(s) + \frac{2}{M_2} \sum_{sa} \Omega^2(s) \bar{\sigma}_{\lambda a}(s) \bar{\sigma}_{\mu a}(s), \quad (\text{A1})$$

where, to ease the notation, we do not indicate the dependence on the training set. The eigenvalue problem can be written as

$$H_{\lambda\mu} v_\lambda^i = c^i v_\lambda^i, \quad (\text{A2})$$

where v^i is the i -th normalized eigenvectors and c^i the corresponding eigenvalue. We thus have

$$\begin{aligned} c^i &= \sum_{\lambda\mu} v_\lambda^i H_{\lambda\mu} v_\mu^i \\ &= \sum_{\lambda\mu} \sum_s \left[\frac{2}{M_1} \sum_\tau v_\lambda^i \bar{f}_{\lambda\tau}(s) \bar{f}_{\mu\tau}(s) v_\mu^i + \frac{2}{M_2} \Omega^2(s) \sum_a v_\lambda^i \bar{\sigma}_{\lambda a}(s) \bar{\sigma}_{\mu a}(s) v_\mu^i \right] \\ &= \sum_s \left[\frac{2}{M_1} \sum_\tau \left(\sum_\lambda v_\lambda^i \bar{f}_{\lambda\tau}(s) \right)^2 + \frac{2}{M_2} \Omega^2(s) \sum_a \left(\sum_\lambda v_\lambda^i \bar{\sigma}_{\lambda a}(s) \right)^2 \right] \geq 0. \end{aligned} \quad (\text{A3})$$

Consequently, the critical manifold is necessarily a minimum (if $c^i > 0 \forall i$) or a collection of minima (if $\exists i$ such that $c^i = 0$). Indeed, since we can have zero eigenvalues, the critical manifold defined by the $\partial G / \partial \theta_\lambda = 0$ condition is not necessarily of dimension zero. Instead of a single point, we can have a minimum- G line, plane, etc. in the space of the model parameters; it immediately follows that such cases correspond to the occurrence of linear dependences in Eq. (18).

Appendix B: Full FM model fitted to TS@10

We give here the complete FM model fitted to TS@10.

TABLE A1. Interactions retained in the short-range part of E_p and E_{sp} , corresponding to the FM model fitted to TS@10. The interactions are described by a polynomial coupling representing the whole SAT that shares the same coupling parameter. All the strain-phonon terms are linear in the strain and quadratic in the atomic displacements, and are given in $\text{eV}/\text{\AA}^2$. As regards the phonon terms, the harmonic ones are given in $\text{eV}/\text{\AA}^2$, 3rd-order ones in $\text{eV}/\text{\AA}^3$, and 4th-order ones in $\text{eV}/\text{\AA}^4$. The terms are given in the order in which they are selected by our automatic fitting procedure. Asterisks mark the terms that we introduce to assure the energy-boundedness of the model.

#	Representative interaction	Coefficient value
1	$(\text{Ti}_y - \text{O2}_y)^2$	1.548×10^1
2	$(\text{O3}_y - \text{Ti}_y[010])(\text{Ti}_y - \text{O3}_y)$	2.406×10^{-1}
3	$\eta_2(\text{O1}_x - \text{O2}_x)(\text{O1}_y - \text{O2}_y)$	6.771
4	$\eta_2(\text{Sr}_x - \text{O3}_x)^2$	-8.876×10^{-1}
5	$\eta_6(\text{Sr}_y - \text{O3}_y[001])(\text{Sr}_x - \text{O3}_x[001])$	-2.226
6	$(\text{Sr}_x - \text{O1}_x)(\text{Sr}_z - \text{O3}_z)$	-1.314
7	$(\text{O3}_x - \text{O3}_x[101])(\text{O3}_x - \text{Ti}_x[110])$	1.606×10^{-2}
8	$(\text{Ti}_x - \text{Sr}_x)(\text{Sr}_x - \text{O2}_x)$	1.490×10^{-1}
9	$(\text{Ti}_x - \text{Ti}_x[100])(\text{Ti}_x - \text{Sr}_x)$	2.764×10^{-2}
10	$(\text{Sr}_x - \text{O2}_x)(\text{Sr}_y - \text{O1}_y)$	4.677×10^{-1}
11	$(\text{Ti}_x - \text{O2}_x)(\text{Ti}_x - \text{O1}_x)$	-7.076×10^{-1}
12	$(\text{Ti}_x - \text{Sr}_x)(\text{Sr}_y - \text{O3}_y)$	1.863×10^{-1}
13	$(\text{Sr}_x - \text{O2}_x)^2(\text{Sr}_z - \text{O3}_z)$	3.243×10^{-1}
14	$(\text{Ti}_z - \text{O2}_z)(\text{Ti}_z[0\bar{1}0] - \text{O2}_z)$ $\times (\text{Ti}_y[0\bar{1}0] - \text{O2}_y)$	-2.760
15	$(\text{Ti}_x - \text{Ti}_x[001])(\text{Ti}_x - \text{Ti}_x[100])$	2.026×10^{-1}
16	$(\text{O1}_y - \text{O2}_y)(\text{O1}_y - \text{O2}_y[010])$	-2.662×10^{-1}
17	$(\text{Ti}_y - \text{Sr}_y)(\text{Sr}_y - \text{O2}_y)$	-1.878×10^{-1}
18	$(\text{Sr}_x - \text{O2}_x)^2(\text{O2}_x - \text{Sr}_x[001])^2$	5.229×10^{-1}
19	$(\text{O1}_y - \text{O3}_y)(\text{Sr}_y - \text{O1}_y)(\text{O1}_x - \text{O3}_x)$	-3.375×10^{-1}
20	$(\text{O2}_z - \text{Ti}_z[100])(\text{O2}_z - \text{O2}_z[11\bar{1}])$	-1.081×10^{-2}
21	$(\text{O1}_z - \text{Sr}_z[010])^2(\text{Sr}_y - \text{O1}_y)^2$	9.529×10^{-1}
22	$\eta_1(\text{Ti}_x - \text{O3}_x)^2$	-8.372
23	$\eta_4(\text{Sr}_z - \text{O1}_z)^2$	-3.203
24	$(\text{Ti}_y - \text{O2}_y)^3$	-8.814
25	$\eta_3(\text{O2}_x - \text{O2}_x[10\bar{1}])^2$	-1.791×10^{-1}
26	$(\text{O1}_x - \text{O1}_x[010])(\text{O1}_x - \text{Ti}_x[010])$	6.514×10^{-2}
27	$(\text{Sr}_y - \text{O2}_y[010])(\text{Sr}_y - \text{Sr}_y[010])$	5.390×10^{-2}
28	$(\text{O1}_z - \text{Ti}_z[010])(\text{Ti}_z - \text{O1}_z)$	8.515×10^{-2}
29	$(\text{Ti}_z - \text{O1}_z[100])(\text{Ti}_z - \text{O1}_z)$	-2.675×10^{-1}
30	$(\text{Sr}_z - \text{O1}_z)(\text{Sr}_y - \text{O1}_y)^3$	8.967×10^{-1}
31	$(\text{O2}_z - \text{O3}_z)(\text{O2}_y - \text{O3}_y)(\text{Sr}_y - \text{O2}_y)$	-3.477×10^{-1}
32	$(\text{Sr}_y - \text{O1}_y)(\text{O1}_y - \text{Ti}_y[011])$	-3.635×10^{-2}
33	$(\text{Ti}_x - \text{O2}_x)^2(\text{O1}_y - \text{O3}_y)^2$	2.332×10^{-1}
34*	$(\text{Ti}_x - \text{O1}_x)^6$	2.595×10^3
35*	$(\text{Ti}_z - \text{Sr}_z)^6$	2.434×10^2

Let us first introduce our notation to describe STO's RS and its distortions; this is the notation used in this Appendix and throughout the paper. In Cartesian coor-

dinates, the cell is given by lattice vectors $\mathbf{a} = a(1, 0, 0)$, $\mathbf{b} = a(0, 1, 0)$, and $\mathbf{c} = a(0, 0, 1)$, where a is the lattice constant given in Angstrom (obtained to be 3.865 \AA from our LDA relaxation). The relative coordinates of the atoms in the cell are: $(0, 0, 0)$ for Sr, $(1/2, 1/2, 1/2)$ for Ti, $(0, 1/2, 1/2)$ for the first oxygen (O1), $(1/2, 0, 1/2)$ for O2, and $(1/2, 1/2, 0)$ for O3. We denote the Cartesian coordinates by x , y , and z ; then, for example, we write Ti_x to denote the displacement along x of the Ti atom in the cell at the origin (i.e., this is the Ti atom located at $a(1/2, 1/2, 1/2)$ in the RS); O2_z would be the displacement along z of the O2 atom in the cell at the origin (i.e., this is the oxygen atom located at $a(1/2, 0, 1/2)$ in the RS). Finally, we use a special notation to refer to atoms located at other lattice cells; hence, for instance, $\text{Sr}_y[110]$ stands for the displacement along y of the Sr atom located at position $a(1, 1, 0)$ in the RS. Finally, the homogeneous deformations of the lattice are given by strains in Voigt notation, following the standard convention.

Table A1 gives the full short-range part of E_p , as obtained by fitting the FM model to the TS@10 training set described in the main text of the paper.

To complete the description of the model, we also need to list the values of the parameters that we compute directly from the LDA calculation and whose corresponding couplings are included in E_{fixed} during the fits. First, we have the long-range dipole-dipole interactions in E_p , which are fully characterized by the tensors in Table A2. Finally, Table A3 gives the LDA-computed elastic tensor.

TABLE A2. Born dynamical effective charges in elemental charge units. We have a 3×3 Born tensor for each atom; however, because of the cubic symmetry of the RS, the tensors are strictly diagonal and, hence, only the diagonal terms are given in the table. The high-frequency dielectric permittivity tensor (which accounts for pure electronic contributions) is isotropic and diagonal for STO's cubic RS, and is thus characterized by a single number $\epsilon_\infty = 6.35$.

	xx	yy	zz
Sr	2.55	2.55	2.55
Ti	7.33	7.33	7.33
O1	-5.77	-2.06	-2.06
O2	-2.06	-5.77	-2.06
O3	-2.06	-2.06	-5.77

TABLE A3. Non-zero elastic constants computed for the cubic phase of STO, given in Voigt notation.

$C_{11} = C_{22} = C_{33} = 388.3 \text{ GPa}$
$C_{12} = C_{13} = C_{23} = C_{21} = C_{31} = C_{32} = 111.4 \text{ GPa}$
$C_{44} = C_{55} = C_{66} = 118.8 \text{ GPa}$

[1] P. Hohenberg and W. Kohn, Physical Review **136**, B864 (1964).

[2] W. Kohn and L. J. Sham, Physical Review **140**, A1133

- (1965).
- [3] R. M. Martin, *Electronic Structure: Basic Theory and Practical Methods* (Cambridge University Press, 2004).
 - [4] S. B. Sinnott and D. W. Brenner, *MRS Bulletin* **37**, 469 (2012).
 - [5] P. García-Fernández, J. C. Wojdel, J. Junquera, and J. Íñiguez, *Physical Review B* **93**, 195137 (2016).
 - [6] A. Kukol, ed., *Molecular Modeling of Proteins* (Springer New York, 2015).
 - [7] J. E. Jones, *Proceedings of the Royal Society of London A: Mathematical, Physical and Engineering Sciences* **106**, 463 (1924).
 - [8] I. D. Brown, *Chem. Rev.* **109**, 6858 (2009).
 - [9] J. M. Perez-Mato, M. Aroyo, A. García, P. Blaha, K. Schwarz, J. Schweifer, and K. Parlinski, *Physical Review B* **70**, 214111 (2004).
 - [10] Y.-H. Shin, V. R. Cooper, I. Grinberg, and A. M. Rappe, *Physical Review B* **71**, 054104 (2005).
 - [11] A. C. T. van Duin, S. Dasgupta, F. Lorient, and W. A. Goddard, *The Journal of Physical Chemistry A* **105**, 9396 (2001).
 - [12] K. V. Jovan Jose, N. Artrith, and J. Behler, *The Journal of Chemical Physics* **136**, 194111 (2012).
 - [13] J. C. Wojdel, P. Hermet, M. P. Ljungberg, P. Ghosez, and J. Íñiguez, *Journal of Physics: Condensed Matter* **25**, 305401 (2013).
 - [14] J. C. Wojdel and J. Íñiguez, *Physical Review Letters* **112**, 247603 (2014).
 - [15] P. Zubko, J. C. Wojdel, M. Hadjimichael, S. Fernandez-Pena, A. Sené, I. Luk'yanchuk, J. Triscone, and J. Íñiguez, *Nature* **534**, 524 (2016).
 - [16] J. F. Nye, *Physical Properties of Crystals: Their Representation by Tensors and Matrices*, Oxford Science Publications (Clarendon Press, 1985).
 - [17] X. Gonze and C. Lee, *Physical Review B* **55**, 10355 (1997).
 - [18] D. Sheppard, P. Xiao, W. Chemelewski, D. D. Johnson, and G. Henkelman, *The Journal of Chemical Physics* **136**, 074103 (2012).
 - [19] L. Xu and W. Zhang, *Analytica Chimica Acta* **446**, 475 (2001).
 - [20] A. Celisse and S. Robin, *Computational Statistics & Data Analysis* **52**, 2350 (2008).
 - [21] L. Prechelt, *Neural Networks* **11**, 761 (1998).
 - [22] D. G. Schlom, L.-Q. Chen, C.-B. Eom, K. M. Rabe, S. K. Streiffer, and J.-M. Triscone, *Annual Review of Materials Research* **37**, 589 (2007).
 - [23] A. Ohtomo and H. Hwang, *Nature* **427**, 423 (2004).
 - [24] E. Bousquet, M. Dawber, N. Stucki, C. Lichtensteiger, P. Hermet, S. Gariglio, J.-M. Triscone, and P. Ghosez, *Nature* **452**, 732 (2008).
 - [25] J. F. Scott, E. K. H. Salje, and M. A. Carpenter, *Physical Review Letters* **109**, 187601 (2012).
 - [26] E. K. H. Salje, O. Aktas, M. A. Carpenter, V. V. Laguta, and J. F. Scott, *Physical Review Letters* **111**, 247603 (2013).
 - [27] F. Lytle, *Journal of Applied Physics* **35**, 2212 (1964).
 - [28] P. A. Fleury, J. F. Scott, and J. M. Worlock, *Physical Review Letters* **21**, 16 (1968).
 - [29] A. M. Glazer, *Acta Crystallographica Section B* **28**, 3384 (1972).
 - [30] K. A. Müller and H. Burkard, *Physical Review B* **19**, 3593 (1979).
 - [31] W. Zhong and D. Vanderbilt, *Physical Review B* **53**, 5047 (1996).
 - [32] W. Zhong and D. Vanderbilt, *Physical Review Letters* **74**, 2587 (1995).
 - [33] A. R. Akbarzadeh, L. Bellaiche, K. Leung, J. Íñiguez, and D. Vanderbilt, *Physical Review B* **70**, 054103 (2004).
 - [34] K. Binder and D. Heermann, *Monte Carlo simulation in statistical physics: an introduction* (Springer-Verlag Berlin Heidelberg, 2010).
 - [35] G. Kresse and J. Furthmüller, *Physical Review B* **54**, 11169 (1996).
 - [36] W. Zhong, D. Vanderbilt, and K. M. Rabe, *Physical Review B* **52**, 6301 (1995).
 - [37] P. E. Blöchl, *Physical Review B* **50**, 17953 (1994).
 - [38] G. Kresse and D. Joubert, *Physical Review B* **59**, 1758 (1999).
 - [39] P. Allen and D. J. Tildesley, *Computer Simulation of Liquids*, Oxford Science Publications (Clarendon Press, 1989).
 - [40] M. Parrinello and A. Rahman, *Journal of Applied Physics* **52**, 7182 (1981).
 - [41] W. Zhong, D. Vanderbilt, and K. M. Rabe, *Physical Review Letters* **73**, 1861 (1994).
 - [42] L. Bellaiche, A. García, and D. Vanderbilt, *Physical Review Letters* **84**, 5427 (2000).
 - [43] I. A. Kornev, S. Lisenkov, R. Haumont, B. Dkhil, and L. Bellaiche, *Physical Review Letters* **99**, 227602 (2007).
 - [44] P. Ghosez, E. Cockayne, U. V. Waghmare, and K. M. Rabe, *Physical Review B* **60**, 836 (1999).
 - [45] U. V. Waghmare and K. M. Rabe, *Physical Review B* **55**, 6161 (1997).
 - [46] H. Krakauer, R. Yu, C. Wang, K. M. Rabe, and U. V. Waghmare, *Journal of Physics: Condensed Matter* **11**, 3779 (1999).
 - [47] X. Wu, D. Vanderbilt, and D. R. Hamann, *Physical Review B* **72**, 035105 (2005).
 - [48] S. C. Abrahams, S. K. Kurtz, and P. B. Jamieson, *Physical Review* **172**, 551 (1968).
 - [49] J. C. Wojdel and J. Íñiguez, *Physical Review B* **90**, 014105 (2014).
 - [50] H. Unoki and T. Sakudo, *Journal of the Physical Society of Japan* **23**, 546 (1967).
 - [51] R. Wahl, D. Vogtenhuber, and G. Kresse, *Physical Review B* **78**, 104116 (2008).
 - [52] J. Íñiguez and D. Vanderbilt, *Physical Review Letters* **89**, 115503 (2002).
 - [53] I. A. Kornev, L. Bellaiche, P.-E. Janolin, B. Dkhil, and E. Suard, *Physical Review Letters* **97**, 157601 (2006).